

*Citation for published version:*

McCormack, J, Hoppel, K, Kuhl, D, de Wit, R, Stober, G, Espy, P, Baker, N, Brown, P, Fritts, D, Jacobi, C, Janches, D, Mitchell, N, Ruston, B, Swadley, S, Viner, K, Whitcomb, T & Hibbins, R 2017, 'Comparison of mesospheric winds from a high-altitude meteorological analysis system and meteor radar observations during the boreal winters of 2009–2010 and 2012–2013', *Journal of Atmospheric and Solar-Terrestrial Physics*, vol. 154, pp. 132-166. <https://doi.org/10.1016/j.jastp.2016.12.007>

*DOI:*

[10.1016/j.jastp.2016.12.007](https://doi.org/10.1016/j.jastp.2016.12.007)

*Publication date:*

2017

*Document Version*

Peer reviewed version

[Link to publication](#)

*Publisher Rights*

CC BY-NC-ND

## University of Bath

**General rights**

Copyright and moral rights for the publications made accessible in the public portal are retained by the authors and/or other copyright owners and it is a condition of accessing publications that users recognise and abide by the legal requirements associated with these rights.

**Take down policy**

If you believe that this document breaches copyright please contact us providing details, and we will remove access to the work immediately and investigate your claim.

# Comparison of mesospheric winds from a high-altitude meteorological analysis system and meteor radar observations during the boreal winters of 2009–2010 and 2012–2013

J. McCormack<sup>1,\*</sup>, K. Hoppel<sup>2</sup>, D. Kuhl<sup>2</sup>, R. de Wit<sup>3</sup>, G. Stober<sup>4</sup>, P. Espy<sup>5</sup>, N. Baker<sup>6</sup>, P. Brown<sup>7</sup>, D. Fritts<sup>8</sup>, C. Jacobi<sup>9</sup>, D. Janches<sup>3</sup>, N. Mitchell<sup>10</sup>, B. Ruston<sup>6</sup>, S. Swadley<sup>6</sup>, K. Viner<sup>6</sup>, T. Whitcomb<sup>6</sup>

---

## Abstract

We present a study of horizontal winds in the mesosphere and lower thermosphere (MLT) during the boreal winters of 2009–2010 and 2012–2013 produced with a new high-altitude data assimilation/forecast system. This system is based on a modified version of the Navy Global Environmental Model (NAVGEN) with an extended vertical domain up to  $\sim 116$  km altitude that assimilates both conventional meteorological observations in the troposphere and satellite-based observations of temperature, ozone and water vapor in the stratosphere and mesosphere. The NAVGEN MLT winds are validated using independent meteor radar wind observations from nine differ-

---

\*Corresponding author

<sup>1</sup>Space Science Division, Naval Research Laboratory, Washington DC, USA

<sup>2</sup>Remote Sensing Division, Naval Research Laboratory, Washington DC, USA

<sup>3</sup>Space Weather Laboratory, NASA Goddard Space Flight Center, Greenbelt, Maryland, USA

<sup>4</sup>Leibniz- Institute for Atmospheric Physics, Rostock University, Kuehlungsborn, Germany

<sup>5</sup>Norwegian University of Science and Technology (NTNU), Trondheim, Norway

<sup>6</sup>Marine Meteorology Division, Naval Research Laboratory, Monterey CA, USA

<sup>7</sup>Department of Physics & Astronomy, University of Western Ontario, London, Ontario, Canada

<sup>8</sup>GATS Inc., Boulder, Colorado, USA

<sup>9</sup>University of Leipzig, Leipzig, Germany

<sup>10</sup>Centre for Space, Atmospheric and Oceanic Science, University of Bath, Bath, UK

ent sites ranging from 69°N –67°S latitude. Time-averaged NAVGEM zonal and meridional wind profiles between 75–95 km altitude show good qualitative and quantitative agreement with corresponding meteor radar wind profiles. Wavelet analysis finds that the 3-hourly NAVGEM and 1-hourly radar winds both exhibit semi-diurnal, diurnal, and quasi-diurnal variations whose vertical profiles of amplitude and phase are also in good agreement. Wavelet analysis also reveals common time-frequency behavior in both NAVGEM and radar winds throughout the Northern extratropics around the times of major stratospheric sudden warmings (SSWs) in January 2010 and January 2013, with a reduction in semi-diurnal amplitudes beginning around the time of a mesospheric wind reversal at 60°N that precedes the SSW, followed by an amplification of semi-diurnal amplitudes that peaks 10–14 days following the onset of the mesospheric wind reversal. The initial results presented in this study demonstrate that the wind analyses produced by the high-altitude NAVGEM system accurately capture key features in the observed MLT winds during these two boreal winter periods.

*Keywords:*

Mesosphere, Winds, Tides, Data assimilation

---

## 1. Introduction

It has become increasingly clear in recent years that day-to-day variability in the composition and structure of the thermosphere and ionosphere is influenced by meteorological variability in the lower atmosphere, i.e., the region of the atmosphere between 0–100 km altitude. This coupling arises from upward propagating planetary waves and tides (both migrating and non-migrating) that are forced in the lower atmosphere and become the dominant drivers of the atmospheric circulation in the equatorial dynamo region between 100–150 km (see, e.g. Akmaev, 2011, and references therein). The vertical propagation of these waves and tides, and their projection onto global resonant modes in the atmospheric circulation, depends strongly on variations in horizontal winds throughout the stratosphere and mesosphere. Consequently, efforts to identify and, ultimately, predict the physical origins of this vertical atmospheric coupling require accurate and detailed wind information extending globally from the surface to the lower thermosphere. Currently, there are relatively few sources of wind observations in the mesosphere and lower thermosphere (MLT). Ground-based wind observations

18 from, e.g., medium frequency radar and meteor radar instruments (Hocking  
19 et al., 2001; Riggan et al., 2003) generally offer excellent temporal sampling  
20 but are limited in their geographical coverage. Direct satellite observations  
21 of winds from space-based platforms (Limpasuvan et al., 2005; Niciejewski  
22 et al., 2006; Baron et al., 2013) are valuable sources of information, but global  
23 coverage can be limited due to a combination of factors involving orbital ge-  
24 ometry, observational method, and mission lifetime. Satellite observations of  
25 temperature and geopotential height have been used to infer horizontal winds  
26 in the stratosphere and mesosphere based on gradient wind balance (Manney  
27 et al., 2008; McLandress et al., 2013; Lieberman et al., 2013). This method  
28 is useful for diagnosing the background flow conditions in the extratropi-  
29 cal MLT that affect the vertical propagation of waves and tides. However,  
30 balanced winds cannot be used to directly determine tidal motions in the  
31 horizontal winds, as these motions are forced by local variations in solar  
32 heating and this forcing violates the assumptions of gradient wind balance.

33 Due to these limitations, most information on coupling between the ther-  
34 mosphere/ionosphere system and meteorological variability in the lower at-  
35 mosphere involving vertical propagation of waves and tides currently does not  
36 come from direct observations, but instead comes from “whole atmosphere”  
37 models that encompass the neutral atmosphere and ionosphere (e.g. Fuller-  
38 Rowell et al., 2010; Jin et al., 2012; Akmaev, 2011; Pedatella and Liu, 2013;  
39 Sassi et al., 2013). An advantage of these models is that they provide a fully  
40 self-consistent set of wind, temperature, and constituent fields throughout  
41 the MLT region where global observations are relatively scarce. However, an  
42 intercomparison among four different whole atmosphere models published  
43 in Pedatella et al. (2014) shows considerable disagreement in the modeled  
44 MLT winds due to the differing physical parameterizations employed in each  
45 model. This disagreement among models highlights the need for accurate,  
46 observations-based global wind information in the MLT region.

47 To address this need, this paper provides a detailed validation of MLT  
48 winds from a new high-altitude meteorological analysis system based on the  
49 Navy Global Environmental Model (NAVGEM) described in Hogan et al.  
50 (2014). The present study builds upon earlier work by Eckermann et al.  
51 (2009) and Hoppel et al. (2013) to develop a forecast/assimilation system  
52 for middle atmosphere research that combines conventional meteorological  
53 observations, space-based temperature and constituent observations in the  
54 stratosphere and mesosphere, and a full-physics general circulation model  
55 (GCM) to generate global synoptic analyses of wind and temperature ex-

56 tending from 0 to  $\sim 100$  km altitude. The present validation study com-  
57 pares NAVGEM MLT wind analyses with independent ground-based meteor  
58 radar wind observations from nine different stations that are listed in Table  
59 1. These comparisons focus on the Northern Hemisphere (NH) winters of  
60 2009-2010 and 2012-2013 when numerous observational studies report large  
61 changes in both MLT dynamics (Stober et al., 2012; Matthias et al., 2013;  
62 de Wit et al., 2015) and ionospheric structure (Chau et al., 2009; Anderson  
63 and Araujo-Pradere, 2010; Pedatella and Forbes, 2010; Jin et al., 2012; Gon-  
64 charenko et al., 2010; Lin et al., 2012; Goncharenko et al., 2013a) following  
65 the onset of major sudden stratospheric warmings (SSWs).

66 Several recent studies using whole atmosphere models link changes in  
67 ionospheric features such as vertical plasma drift and total electron content to  
68 changes in the global circulation of the stratosphere and mesosphere during  
69 an SSW that modify the upward propagation of both migrating and non-  
70 migrating tides into the equatorial dynamo region (Fuller-Rowell et al., 2010;  
71 Jin et al., 2012; Pedatella and Liu, 2013; Sassi et al., 2013). A SSW is  
72 caused by the rapid amplification of planetary wave (PW) activity in the  
73 extratropical winter stratosphere that produces increased westward drag on  
74 the eastward polar night jet and a resulting increase in descent over the  
75 winter pole that produces anomalously warm temperatures through adiabatic  
76 heating. The effects of the increased PW drag on the polar jet first appear  
77 in the mesosphere and can descend into the stratosphere over the course of  
78 several days. In the case of a major SSW, the increased PW drag is strong  
79 enough to produce a reversal in the direction of the polar jet (from eastward  
80 to westward) down to  $\sim 30$  km altitude. This reversal limits the upward  
81 propagation of planetary waves into the stratosphere, and also acts to favor  
82 vertical propagation of eastward propagating gravity waves (GWs) into the  
83 mesosphere, resulting in a diminished polar descent and a net cooling in the  
84 mesospheric region overlying the SSW. As the eastward polar jet begins to  
85 recover, increased downwelling appears over the pole in the mesosphere to  
86 form an “elevated stratopause” (e.g. Siskind et al., 2010).

87 As Figure 1 shows, these characteristic dynamical signatures of a major  
88 SSW in zonal mean zonal wind and zonal mean temperature are captured in  
89 the NAVGEM analyses for the 2009-2010 and 2012-2013 NH winters. While  
90 it is common practice to describe the timing of an SSW in terms of the zonal  
91 wind reversal at, e.g.,  $60^\circ\text{N}$  and 10 hPa ( $\sim 30$  km altitude), in the present  
92 study we will focus instead on the date when a sustained ( $> 5$  days) reversal  
93 of mesospheric winds from westerly to easterly at  $60^\circ\text{N}$  begins. This is done

94 in order to better relate variability in periodic MLT wind variations (e.g.,  
95 tides) to the dramatic reversals in background MLT winds that precede the  
96 SSW; similar methods have also been employed in recent studies examining  
97 the mesospheric response during SSWs (Stober et al., 2012; Matthias et al.,  
98 2012; Stray et al., 2015; Limpasuvan et al., 2016). During the 2010 SSW  
99 event, which was characterized by a rapid amplification of planetary wave 1 at  
100 10 hPa in late January (Goncharenko et al., 2013a), the NAVGEM analyses in  
101 Fig. 1 indicate this mesospheric reversal began on 27 January, approximately  
102 2 weeks prior to the sustained stratospheric zonal wind reversal at 60°N and  
103 10 hPa that began on 9 February (Kuttippurath and Nikulin, 2012). During  
104 the 2013 SSW, which was characterized by a rapid amplification of planetary  
105 wave 2 at 10 hPa in early January, the mesospheric wind reversal at 60°N  
106 begins on 7 January, nearly the same time that the stratospheric jet reversal  
107 first appears at 10 hPa.

108 There is both modeling and observational evidence that these changes in  
109 PW drag, GW drag, and the meridional circulation associated with a major  
110 SSW can exert an impact on the dynamics of the MLT that extends to the  
111 equatorial regions and possibly the Southern Hemisphere as well (see, e.g.  
112 Limpasuvan et al., 2016, and references therein). One common feature that  
113 has been identified in several studies is the amplification of the semi-diurnal  
114 westward migrating zonal wave number 2 (SW2) tide after the onset of the  
115 SSW (Wang et al., 2011; Jin et al., 2012; Goncharenko et al., 2013b; Pedatella  
116 and Liu, 2013; Limpasuvan et al., 2016). A possible mechanism to explain  
117 this behavior is that changes in the spatial distribution of stratospheric ozone  
118 heating caused by meridional circulation anomalies related to the SSW alter  
119 the forcing of the migrating semi-diurnal tide (Goncharenko et al., 2012). An-  
120 other possible mechanism is that changes in vorticity throughout the tropical  
121 stratosphere and mesosphere that affect the vertical propagation of migrating  
122 tides into the thermosphere (Sassi and Liu, 2014). The search for a definitive  
123 mechanism (or mechanisms) to explain how the onset of an SSW impacts the  
124 behavior of SW2 is complicated by the fact that there is broad disagreement  
125 in the amplitude of the SW2 response to an SSW among whole atmosphere  
126 models (Pedatella et al., 2014, their Figure 10).

127 The goal of the present study is to evaluate the behavior of MLT winds  
128 during two NH winter periods when major SSWs occurred through detailed  
129 comparisons of NAVGEM analyzed winds with independent meteor radar  
130 winds for the 2009-2010 and 2012-2013 winters. The results of this valida-  
131 tion study show that high-altitude NAVGEM analyses provide an accurate

132 description of global MLT winds that can be used to inform future studies on  
133 coupling between the lower atmosphere and ionosphere through modulation  
134 of tides.

135 Section 2 provides a description of the high-altitude NAVGEM system as  
136 well as the nine ground-based meteor radar wind records used for validating  
137 the NAVGEM results. Section 3 presents detailed comparisons of the day-  
138 to-day variations in zonal and meridional winds from both NAVGEM and  
139 meteor radar observations. Section 4 examines vertical profiles of tidal am-  
140 plitude and phase from NAVGEM and radar winds. Section 5 compares the  
141 temporal variations in the dominant planetary wave and tidal components  
142 derived from the NAVGEM and meteor radar winds. Section 6 summarizes  
143 the major findings and discusses their significance for improving our under-  
144 standing of how meteorological variability in the lower atmosphere influences  
145 ionospheric conditions during recent SSWs.

## 146 **2. Data Description**

147 This section presents descriptions of both the high-altitude NAVGEM  
148 analyses and the meteor radar observations that are used to provide informa-  
149 tion on tidal variations in MLT winds around the times of SSWs in January  
150 2010 and 2013.

### 151 *2.1. High-altitude NAVGEM*

152 The high-altitude NAVGEM system used in the present study provides  
153 atmospheric specifications of wind, temperature, and composition from the  
154 surface to  $\sim 100$  km altitude that can be used to constrain lower atmospheric  
155 variability in whole atmosphere models. It is based on the operational fore-  
156 cast/assimilation system described in Hogan et al. (2014), which combines  
157 a semi-Lagrangian/semi-implicit (SL/SI) global spectral forecast model with  
158 a four-dimensional variational (4DVAR) data assimilation algorithm. The  
159 4DVAR component of NAVGEM, known as the NRL Atmospheric Varia-  
160 tional Data Assimilation System with Accelerated Representer (NAVDAS-  
161 AR), processes over 1.5 million observations every 6-hour assimilation cycle  
162 from a variety of *in-situ* sources (e.g., surface reports, radiosondes, ship and  
163 aircraft data) and satellite-based remote sensing data (e.g., radiance mea-  
164 surements from infrared and microwave sensors, global positioning system  
165 radio occultations, cloud track winds) that are available operationally. The

166 high-altitude version of NAVGEM used in the present study includes sev-  
167 eral additional features that are key to producing accurate meteorological  
168 analyses in the MLT region, which we describe here.

169 First, the vertical domain of the forecast model was extended from its cur-  
170 rent operational 60-level (L60) configuration with a top pressure of 0.04 hPa  
171 to a 74-level (L74) configuration with top pressure of  $6 \times 10^{-5}$  hPa ( $\sim 116$  km  
172 altitude) and a vertical spacing of  $\sim 2$  km in the stratosphere and mesosphere.  
173 The model employs a hybrid vertical coordinate that is terrain-following near  
174 the surface and smoothly transitions to pure pressure levels in the lower  
175 stratosphere (Eckermann et al., 2009). Enhanced diffusion is applied in the  
176 top three model levels to limit wave reflection, producing an effective “sponge  
177 layer” above 100 km altitude. To avoid the possibility of the analyses being  
178 affected by this sponge layer, we only report NAVGEM results below the  
179 100 km level.

180 Next, virtual potential temperature  $\theta_v$  was replaced with a perturbation  
181 virtual potential temperature  $\theta'_v$  as the prognostic thermodynamic variable in  
182 the L74 NAVGEM forecast model. This change addresses stability issues that  
183 arose in earlier versions of NAVGEM related to the use of the SL/SI method  
184 with a conservative thermodynamic variable (see, e.g. Staniforth et al., 2006;  
185 Juang, 2011). These issues were traced to the vertical advection of  $\theta_v$  related  
186 to gravity wave activity; in certain cases excessive variability of the local flow  
187 led to violations of the Lipschitz condition (Smolarkiewicz and Pudykiewicz,  
188 1992). For NWP purposes, stability at larger time steps ( $> 5$  min) had to  
189 be maintained through either strong implicit biasing (also called decentering  
190 or off-centering) of the SI scheme or imposed numerical diffusion, measures  
191 that smooth the local flow and reduce the accuracy of the method.

192 To improve both the stability and accuracy of the SL/SI scheme, the L74  
193 NAVGEM forecast model uses the perturbation virtual potential tempera-  
194 ture  $\theta'_v = \theta_v - \theta_0$  as the prognostic thermodynamic variable, where  $\theta_0$  is  
195 a climatological basic state potential temperature. This method allows the  
196 SL/SI scheme to sufficiently damp the gravity waves by extracting the ver-  
197 tical advection of  $\theta_0$  from the trajectory calculation. In the L74 NAVGEM  
198 forecast model, the vertical profile of  $\theta_0$  is defined as a diagnostic function  
199 of Exner pressure calculated using a nonlinear regression fit to a combina-  
200 tion of the 1976 US Standard atmosphere below the 10 hPa level ( $\sim 30$  km  
201 altitude) and a global mean temperature profile based on ten years of obser-  
202 vations from the Sounding of the Atmosphere using Broadband Emission of  
203 Radiation (SABER) instrument on the NASA TIMED satellite (Rezac et al.,

204 2015) above the 10 hPa level. Dynamical core tests have shown that use of  
205 the perturbation virtual potential temperature based on this  $\theta_0$  profile pro-  
206 vides stable model performance throughout the vertical domain of the L74  
207 model over a wide range of horizontal resolutions and model time steps.

208 Three data sources for the stratosphere, mesosphere, and lower ther-  
209 mosphere were also added to the input stream for the high-altitude L74  
210 NAVGEM system following procedures described in Eckermann et al. (2009)  
211 and Hoppel et al. (2013): (1) profiles of temperature, ozone mixing ratio, and  
212 water vapor mixing ratio from the Version 3.3 retrievals of the Microwave  
213 Limb Sounder (MLS) on board the NASA Aura satellite (Livesey et al.,  
214 2011); (2) temperature profiles from version 2.0 SABER retrievals; and (3)  
215 microwave radiances from the upper atmosphere sounding (UAS) channels  
216 of the Special Sensor Microwave Imager/Sounder (SSMIS) on the F16, F17,  
217 and F18 series of Defense Meteorological Satellite Program (DMSP) plat-  
218 forms (Swadley et al., 2008). The MLS constituent profiles are assimilated  
219 into the system’s prognostic ozone and water vapor fields, which are used in  
220 the forecast model’s radiative heating calculations.

221 Finally, a new hybrid data assimilation method that linearly combines  
222 static NAVDAS-AR background error covariance estimates with covariances  
223 derived from an 80-member flow-dependent ensemble of instantaneous 6-hour  
224 forecasts (Kuhl et al., 2013) was introduced into this version of the high-  
225 altitude NAVGEM forecast/assimilation system. This hybrid approach has  
226 been shown to improve high-altitude analyses by providing more realistic  
227 estimates of background (i.e., forecast model) uncertainty in atmospheric  
228 state variables, which in turn allows for fewer rejected observations and thus  
229 a more observationally-constrained product compared to the conventional  
230 approach that uses static error covariances (Kuhl et al., 2013).

231 Figure 2 plots an example of the geographic coverage provided by the  
232 MLS, SABER, and UAS observations over a 6-hour interval that are used  
233 as input for the high altitude NAVGEM system. MLS profiles of tempera-  
234 ture, ozone, and water vapor are assimilated at pressure levels between 100  
235 – 0.002 hPa ( $\sim 16 - 90$  km altitude) over the latitude range from  $82^\circ\text{S}$  to  
236  $82^\circ\text{N}$ . SABER temperature profiles are assimilated over the 100 – 0.0002  
237 hPa range ( $\sim 16 - 105$  km). The latitude coverage of the SABER instrument  
238 continuously switches between a “north-viewing” mode ( $52^\circ\text{S} - 83^\circ\text{N}$ ) and a  
239 “south-viewing” mode ( $82^\circ\text{S} - 52^\circ\text{N}$ ) every 60 days. During the 2009-2010  
240 winter, SABER switched from south-viewing mode to north-viewing mode  
241 on 11 January 2010 and remained there until 15 March. During the 2012-

242 2013 winter, SABER switched from south-viewing to north-viewing mode on  
243 7 January 2013, and returned to south-viewing mode on 11 March. SSMIS  
244 UAS microwave radiances from channels 19, 20, and 21 on the polar orbit-  
245 ing F16, F17, and F18 platforms are assimilated throughout the two NH  
246 winter periods. The weighting functions of these three channels lie between  
247 approximately 50–80 km altitude and are vertically deep, spanning up to 20  
248 km altitude at full width of half maximum (see, e.g., Figure 1 of Hoppel  
249 et al., 2013). The altitude of peak sensitivity varies by as much as 10 km  
250 with geomagnetic activity due to Zeeman splitting, which is accounted for  
251 in preprocessing of UAS radiances prior to assimilation in NAVGEM using  
252 a fast radiative transfer model (Bell et al., 2008; Han et al., 2010).

253 For the 2009-2010 and 2012-2013 winter cases, the high-altitude NAVGEM  
254 system was initialized on 5 November 2009 and 15 November 2013, respec-  
255 tively, to allow a 2–3 week “spin-up” period for the satellite radiance varia-  
256 tional bias correction scheme (Hogan et al., 2014). These initialization dates  
257 were determined by the availability of archived operational NAVGEM atmo-  
258 spheric analyses. Lower boundary conditions were specified using archived  
259 analyses of sea surface temperatures and sea ice concentrations provided  
260 by the Navy Fleet Numerical Meteorology and Oceanography Center (FN-  
261 MOC). For the current study, the L74 NAVGEM forecast model employed a  
262 triangular spectral truncation at wave number 119 (T119), giving an effec-  
263 tive horizontal grid spacing of  $1^\circ$  in latitude and longitude. The model time  
264 step is 15 minutes. The ensemble of forecasts used within the hybrid 4DVAR  
265 system were carried out at T47 ( $2.5^\circ$  horizontal grid spacing). The stan-  
266 dard NAVGEM assimilation cycle is every 6 hours, producing global synoptic  
267 analyses of winds, temperature, geopotential height, ozone, water vapor, and  
268 derived state variables such as horizontal divergence and vorticity four times  
269 daily at 00UTC, 06UTC, 12UTC, and 18UTC on a  $1^\circ$  latitude/longitude grid.  
270 Here we augment this output using 3-hour T119 NAVGEM forecasts initial-  
271 ized from each of these 6-hourly analyses that are generated each assimilation  
272 cycle as part of the 4DVAR system. In doing so, we obtain corresponding  
273 output fields at 03UTC, 09UTC, 15UTC, and 21UTC that, when combined  
274 with the 6-hourly analyses, gives a net sampling frequency of 3 hours capable  
275 of resolving waves up to the Nyquist frequency of 4 cpd.

276 For comparison with the meteor radar winds, vertical profiles of high-  
277 altitude NAVGEM analyzed winds are converted from the model vertical  
278 grid to a geometric altitude grid using analyzed geopotential heights as in  
279 Eckermann et al. (2009). Figure 3 compares time series of NAVGEM 3-

280 hourly analysis/forecast meridional winds at 87–88 km with corresponding  
281 hourly meteor radar winds from 4 different sites: Trondheim, Juliusruh, As-  
282 cension Island and Tierra del Fuego. These comparisons demonstrate that  
283 the 3-hourly NAVGEM successfully captures key periodic structures in the  
284 observed meridional winds over a wide range of latitude. A detailed analy-  
285 sis of the temporal variability in the NAVGEM and meteor radar winds is  
286 presented in Section 4.

## 287 *2.2. Meteor radar observations*

288 The present study analyzes zonal and meridional winds obtained from  
289 nine separate radar sites listed in Table 1. The specific technical details of  
290 each radar are summarized in Table 2.

291 The meteor radar data can be divided into two groups based on the data  
292 processing used to derive the winds. The first group consists of data from  
293 the Esrange, Trondheim, Bear Lake, Ascension Island, Tierra del Fuego and  
294 Rothera sites. For these stations, winds have been determined using the  
295 method described in Fritts et al. (2010a, and references therein), to produce  
296 vertical profiles of hourly zonal and meridional winds between 75–80 km, 80–  
297 84 km, 84–86 km, 86–88 km, 88–90 km, 90–92 km, 94–96 km, and 96–100  
298 km. This method uses a least squares fit to the measured radial velocities  
299 of meteor trails when a minimum of 7 meteors are present in each time-  
300 altitude interval. In addition, the double loop system described in Hocking  
301 et al. (2001) was implemented to discard large outliers in the radial velocities  
302 that are not representative of the mean winds. The resulting wind estimates  
303 are assigned to the middle of each time-altitude interval, i.e., observations  
304 from 04–05 UTC and 90–92 km altitude are assigned to 0430 UTC and 91  
305 km altitude. The variable altitude spacing corrects for the change of meteor  
306 counts as a function of altitude.

307 The wind retrievals from Andenes, Juliusruh, Collm and the Canadian  
308 Meteor Orbit Radar (CMOR) are based on an updated wind fitting algorithm  
309 that accounts for error propagation of each individual radial velocity uncer-  
310 tainty and the angular error of the interferometer (Stober et al., 2012). The  
311 instantaneous three-dimensional wind vector  $\mathbf{V} = (u, v, w)$  is obtained using  
312 a constrained least squares solution where the vertical and time derivatives  
313 of each wind vector component  $(u, v, w)$  are assumed to be constant. It  
314 is assumed that the vertical wind is small ( $w \approx 0$ ), which is justified consider-  
315 ing the large observation volume of 600 km in diameter of the meteor radars.  
316 This analysis is applied to a minimum of 5 meteors within each time-altitude

317 interval. Wind estimates from all four sites are processed using 1 km alti-  
 318 tude gates with oversampling of 3 km and 2 hours in time to produce hourly  
 319 time series of zonal and meridional winds at 2 km intervals between 70–110  
 320 km altitude. Each meteor is weighted by a Gaussian kernel depending on  
 321 its vertical distance from the altitude reference grid as well as by its time  
 322 difference from the reference value within each time interval.

323 The numerical methods used in this study to characterize tidal variability  
 324 in MLT winds (described in the following section) require continuous time  
 325 series. Table 1 lists the time periods over which the meteor radar winds from  
 326 each station are analyzed with these methods. These periods were selected  
 327 to avoid extended gaps (one day or longer) in an individual site’s data record.  
 328 Within these selected periods, smaller data gaps (typically 2–3 hours) occur  
 329 sporadically due to, e.g., low meteor rate counts or instrumental issues. To  
 330 obtain a continuous data record, we perform a linear interpolation across  
 331 these smaller gaps to fill in the missing data.

### 322 3. Analysis of temporal variability in MLT winds

333 To characterize the dominant modes of temporal variability in the NAVGEM  
 334 and meteor radar time series used in this study, we use the  $S$ -transform  
 335 method described in Stockwell et al. (1996), which is an extension of a contin-  
 336 uous wavelet transform analysis that utilizes an adjustable Gaussian window.  
 337 For a continuous time series  $u(t)$  with a corresponding Fourier transform  
 338  $\hat{u}(\alpha)$ , the complex  $S$ -transform can be expressed as

$$S(\tau, f) = \int_{-\infty}^{+\infty} \hat{u}(\alpha + f) e^{-2(\frac{\pi k \alpha}{f})^2} e^{i2\pi \alpha \tau} \quad (1)$$

339 where  $\tau$  and  $f$  represent the time and frequency dependence of the  $S$ -transform,  
 340 respectively, and  $\alpha$  is the frequency associated with the Fourier transform of  
 341  $u(t)$ . The width of the Gaussian window, expressed as  $\frac{\pi k \alpha}{f}$ , is a function of  
 342 frequency  $f$  that can be adjusted by the choice of scaling factor  $k > 0$  (Ven-  
 343 tosa et al., 2008, their equation 2). Values of  $0 < k < 1$  increase the temporal  
 344 resolution of  $S$  at the expense of spectral resolution, whereas values of  $k > 1$   
 345 increase the spectral resolution at the expense of the temporal resolution.  
 346 One advantage of the  $S$ -transform is that it can provide information on the  
 347 temporal variability of both the magnitude and phase of each frequency com-  
 348 ponent in the time series  $u(t)$  without *a priori* assumptions about the nature

349 of the variability in the time series. This is in contrast to conventional fitting  
 350 methods often used to extract tidal signals from MLT wind records, which  
 351 assume the presence of a dominant mode (or modes) of variability through-  
 352 out the entire data record. Another advantage of the  $S$ -transform is that,  
 353 unlike other wavelet techniques, the time-integrated complex  $S$ -transform  
 354 yields exactly the Fourier spectrum, i.e.,

$$\langle S \rangle = \int_{-\infty}^{+\infty} S(\tau, f) d\tau = \hat{u}(f). \quad (2)$$

355 This property is helpful for comparison of  $S$ -transform results with one- and  
 356 two-dimensional Fourier analyses commonly used to identify tidal and plan-  
 357 etary wave signals in MLT winds (e.g., McCormack et al., 2010, 2014).

358 In the present study, the  $S$ -transform is applied to time series of zonal and  
 359 meridional winds from both 3-hourly NAVGEM output and 1-hourly meteor  
 360 radar observations. To isolate the temporal variability of specific periodic  
 361 features such as tides, instantaneous values of wave amplitude  $|S|$  and phase  
 362  $\phi$  are calculated as a function of frequency and time as

$$|S(\tau, f)| = \sqrt{\text{Re}(S)^2 + \text{Im}(S)^2} \quad \phi(\tau, f) = \arctan \left[ \frac{\text{Im}(S)}{\text{Re}(S)} \right]. \quad (3)$$

363 Although the time-integrated complex  $S$ -transform is equivalent to the Fourier  
 364 transform over the time window being analyzed for any value of the scaling  
 365 factor  $k$ , instantaneous values of the amplitude  $|S|$  are sensitive to the choice  
 366 of  $k$ . To illustrate this sensitivity, Figure 4 plots values of  $|S|$  as a function of  
 367 time and frequency obtained from hourly Ascension Island meridional wind  
 368 time series at 87 km for February 2010 using three different values of  $k$ . As  
 369 Figure 4a shows, the winds exhibit a strong 2-day oscillation in early Febru-  
 370 ary that transitions to a combination of diurnal and semi-diurnal variability  
 371 later in the month. This transition can be clearly seen in Fig. 4b, 4c, and 4d,  
 372 which plot values of  $|S|$  using factors of  $k = 1$ ,  $k = 1$ , and  $k = 1.5$ , respec-  
 373 tively. Wave amplitudes using  $k = 0.5$  (Fig. 4b) have higher time resolution  
 374 at the expense of frequency resolution, while amplitudes using  $k = 1.5$  (see  
 375 Fig. 4d) have higher frequency resolution at the expense of temporal resolu-  
 376 tion. A comparison of the wave spectra derived using a fast Fourier transform  
 377 or FFT (Fig. 4e-f, black curves) with values of  $\langle S \rangle$  (Fig. 4e-f, orange dashed  
 378 curves) shows that the time-averaged complex  $S$ -transform matches the FFT  
 379 spectra regardless of the value of scaling factor  $k$ . However, the choice of  $k$

380 does affect the spectral shape of instantaneous values of  $|S|$ , which can be  
381 seen in the monthly mean values of  $|S|$  plotted in Fig. 4e-f (gray curves).

382 The results plotted in Figure 4 illustrate the trade-off between time and  
383 frequency resolution of  $|S|$  associated with the choice of scaling factor  $k$ .  
384 Based on these results, and on examination of  $S$ -transform spectra derived  
385 from the other stations listed in Table 1 (not shown), we adopt a scaling  
386 factor of  $k = 1.0$  in order to capture the temporal variability in  $|S|$  (see Fig.  
387 4c) while also preserving the main spectral characteristics in time-averaged  
388 values of  $|S|$  that are present in the FFT and  $\langle S \rangle$  results (Fig. 4f), i.e., the  
389 peak amplitudes at 0.5 cpd, 1 cpd, and 2 cpd.

## 390 4. Results

391 This section presents a detailed comparison of high-altitude NAVGEM  
392 analyzed winds and meteor radar wind observations in the MLT. First, we  
393 examine the time variations in vertical profiles of zonal and meridional winds  
394 for each station location and time period listed in Table 1. Next, we compare  
395 the monthly mean amplitudes and phases of the main periodic features (i.e.,  
396 diurnal and semi-diurnal tide and 2-day wave) in the NAVGEM and meteor  
397 radar winds at each location using the  $S$ -transform. We then analyze the  
398 time variations in these periodic features during the SSWs in January 2010  
399 and January 2013 to determine how well the NAVGEM analyses capture the  
400 observed variations in the MLT winds.

### 401 4.1. Vertical profiles of $U$ and $V$

402 Figures 5–18 plot the time variations in the vertical profiles of meridional  
403 wind ( $V$ ) and zonal wind ( $U$ ) from the hourly meteor radar observations (left  
404 column) and the corresponding 3-hourly NAVGEM analyzed winds (center  
405 column); periods of missing data are indicated with gray contours. The right  
406 column in Figs. 5–18 plots the vertical profiles of the time-averaged winds for  
407 each station and month. Where a complete month’s worth of meteor radar  
408 observations are available, the time average is simply the monthly mean.  
409 Where there are extended data gaps of 1 day or longer, the time averaging is  
410 carried out over the longest continuous time interval within a given month.  
411 For example, Figure 5 plots the zonal and meridional wind profiles at Andenes  
412 for the December 2009 – February 2010 period. Due to missing meteor radar  
413 data over December 18–19 (Fig. 5, upper left), the wind profiles plotted in  
414 the upper right panel of Fig. 5 represent the time mean from 1–17 December

415 2009 (see also Table 1). Similarly, due to missing data over the January  
416 26–28 and February 9–10 periods, the time averaged wind profiles for these  
417 months are limited to 1–25 January and 12–28 February, respectively.

418 Overall, there is good agreement between the meteor radar winds and  
419 NAVGEM analyzed winds at Andenes during the winters of 2009–2010 and  
420 2012–2013 plotted in Figures 5 and 6, respectively. The dominant periodic  
421 feature throughout the winter is the semi-diurnal tide in both meridional and  
422 zonal winds. The semi-diurnal tide also dominates the wind profiles at the  
423 nearby Trondheim station during the 2012–2013 winter shown in Figure 7.  
424 In addition to the semi-diurnal tide, there is also sporadic low-frequency vari-  
425 ability with apparent periods of  $\sim 5$ –10 days in both NAVGEM and meteor  
426 radar winds at Andenes and Trondheim. The time mean profiles of  $U$  and  $V$   
427 in Figs. 5, 6, and 7 are in good agreement overall, although we note that the  
428 NAVGEM zonal winds often exhibit a westerly (i.e., positive) bias of 5–10  $\text{m s}^{-1}$   
429 relative to the meteor radar winds. For reference, typical values of the  
430 corresponding standard deviations in the time means of  $U$  and  $V$  over these  
431 periods range from  $\sim 20 \text{ m s}^{-1}$  at 70 km to  $\sim 40 \text{ m s}^{-1}$  at 90 km, regardless  
432 of whether the time period considered is a full month or only 2–3 weeks. Al-  
433 though the differences between the time mean NAVGEM and meteor radar  
434 wind profiles are small compared to these standard deviations, these differ-  
435 ences can be useful for identifying possible systematic biases in NAVGEM  
436 winds that will need to be studied (and rectified) in the future.

437 Figures 8 and 9 compare  $U$  and  $V$  profiles from NAVGEM and from the  
438 Juliusruh meteor radar for the 2009–2010 and 2012–2013 winters, respec-  
439 tively. The wind profiles are characterized by a combination of semi-diurnal  
440 and low-frequency variations, similar to the Andenes and Trondheim wind  
441 profiles. These same characteristics are also seen in wind profiles from the  
442 nearby Collm site for the two winters, which are plotted in Figures 10 and  
443 11. The mean NAVGEM  $U$  and  $V$  profiles in Figs. 8–11 are in good overall  
444 agreement with the mean meteor radar winds; some exceptions are seen in  
445 the December 2009 mean profiles of  $V$  (Figs. 8 and 10, top right) and the  
446 February 2010 mean profiles of  $U$  (Figs. 8 and 10, bottom right), where the  
447 NAVGEM winds above 85 km are 15–20  $\text{ms}^{-1}$  stronger than the meteor radar  
448 winds. The NAVGEM winds capture the observed interannual variations in  
449 the mean wind profiles at Juliusruh and Collm between the two winter cases.  
450 Specifically, both data sets show stronger westerly flow between 78–85 km  
451 in January and February 2013 (Figs. 9 and 11) compared to January and  
452 February 2010 (Figs. 8 and 10).

453 Figures 12 and 13 plot the  $U$  and  $V$  profiles from NAVGEM analyses  
454 and CMOR observations for the 2009–2010 and 2012–2013 winters, respec-  
455 tively. Again, a combination of semi-diurnal and longer-period oscillations  
456 are evident. The NAVGEM and CMOR meridional wind profiles during both  
457 winters are in good agreement. The zonal wind profiles exhibit considerable  
458 differences, particularly between 78–85 km where the NAVGEM westerly  
459 winds are 20–25 m s<sup>-1</sup> stronger than the CMOR winds during the month of  
460 December 2009 (Fig. 12), and throughout the December 2010 to February  
461 2013 period (Fig. 13).

462 Figures 14 and 15 plot the  $U$  and  $V$  profiles from NAVGEM analyses and  
463 meteor radar observations at Bear Lake for the 2009–2010 and 2012–2013  
464 winters, respectively. The Bear Lake records contain numerous gaps, partic-  
465 ularly above 90 km throughout the 2009–2010 winter and during January and  
466 February of 2013. There are also similar data gaps below 82 km throughout  
467 the 2012–2013 winter. At altitudes between 80–90 km where both NAVGEM  
468 and Bear Lake meridional wind profiles are available, the monthly mean  $V$   
469 values during both winters (Figs. 14 and 15) are in good agreement. The  
470 monthly mean  $U$  profiles during the 2009–2010 winter exhibit considerable  
471 differences, particularly below 85 km, where the NAVGEM westerly winds  
472 are 10–20 m s<sup>-1</sup> stronger than the Bear Lake winds during the months of  
473 December 2009 and January 2010 (Fig. 14). The monthly mean  $U$  profiles  
474 for the 2012–2013 winter (Fig. 15) are in good agreement during December  
475 and January. In February, the NAVGEM mean zonal winds are up to 20 m  
476 s<sup>-1</sup> weaker than the radar winds between 80–90 km.

477 In addition to the six NH stations discussed above, this study also com-  
478 pares NAVGEM analyzed winds with meridional and zonal wind profiles from  
479 three Southern Hemisphere (SH) stations during the 2009–2010 and 2012–  
480 2013 winters (see Table 1). Examining the winds in both hemispheres during  
481 these two winters provides an excellent opportunity to validate the global  
482 behavior of NAVGEM winds around the time of SSWs in January 2010 and  
483 January 2013.

484 Figure 16 plots  $U$  and  $V$  profiles over Ascension Island for the period from  
485 1 January – 31 March 2010. In contrast to the NH stations where the semi-  
486 diurnal oscillation dominates, the NAVGEM and meteor radar meridional  
487 winds at this tropical location (8.0°S, 14.4°W) exhibit a combination of 2-  
488 day, diurnal, and semi-diurnal variability (see also Fig. 4). The monthly  
489 mean profiles of  $V$  from NAVGEM analyses and meteor radar observations  
490 are in overall good agreement at this location. A comparison of the monthly

491 mean  $U$  profiles in Fig. 16 shows that the NAVGEM zonal winds have a  
492 strong westerly bias of 20–40  $\text{m s}^{-1}$  in February and March 2010.

493 Figures 17 and 18 offer comparisons of NAVGEM and meteor radar winds  
494 at the higher-latitude SH (summer) locations of Tierra del Fuego and Rothera  
495 during 2012–2013 winter period, respectively. Due to missing data in January  
496 2013,  $U$  and  $V$  profiles from Tierra del Fuego are compared with NAVGEM  
497 winds for December 2012, February 2013, and March 2013 (Fig. 17). At  
498 this location,  $S$ -transform analysis finds that the main periodic variations in  
499 both  $U$  and  $V$  are at 1 cpd, consistent with the diurnal tide. There is also  
500 lower frequency variability in  $V$  with a mean period of 2.5 cpd. We note that  
501 the amplitude of the diurnal variation in  $V$  ( $\sim 15 \text{ m s}^{-1}$ ) is roughly one-half  
502 the amplitude of the variation at the other extratropical NH and tropical  
503 SH stations. The monthly mean  $U$  and  $V$  profiles at Tierra del Fuego from  
504 NAVGEM and meteor radar wind observations are in good qualitative and  
505 quantitative agreement for these three months. In particular, the NAVGEM  
506 zonal winds capture the sharp vertical gradient in  $U$  observed between 82–  
507 95 km in December 2012 and February 2013.

508 Figure 18 plots  $U$  and  $V$  over Rothera during the period from December  
509 2012 to February 2013. At this high southern latitude, the wind variations  
510 consist mainly of a relatively weak ( $\sim 10 \text{ m s}^{-1}$ ) diurnal variation. Due to  
511 large data gaps in the meteor radar record at this location during December  
512 2012 and early January 2013, only mean profiles of  $U$  and  $V$  from the meteor  
513 radar observations for 15–31 January and 1–28 February of 2013 are plotted  
514 in Fig. 18. Overall, the NAVGEM mean  $U$  and  $V$  profiles for January and  
515 February 2013 are in good agreement with the meteor radar observations  
516 between 80–90 km.

517 In summary, these initial comparisons of the  $U$  and  $V$  profiles from  
518 NAVGEM and meteor radar wind observations over the 2009–2010 and 2012–  
519 2013 NH winter periods demonstrate that the NAVGEM analyses accurately  
520 capture the main characteristics in the MLT winds at these nine locations,  
521 both in terms of the periodic variations and of the time-averaged flow. The  
522 main deficiency in the NAVGEM winds appears to be a westerly bias of  
523 approximately 10–20  $\text{m s}^{-1}$  in mean zonal wind profiles below  $\sim 85$  km at  
524 NH midlatitudes (e.g., Figs. 12, 13, and 14), and a stronger westerly bias  
525 of 20–40  $\text{m s}^{-1}$  during February and March of 2013 at the SH tropical sta-  
526 tion of Ascension Island (Fig. 16). These types of biases in the NAVGEM  
527 zonal winds could arise from systematic errors in the physical parameter-  
528 izations used in the forecast model component of NAVGEM (e.g., gravity

529 wave drag). A more systematic validation of global zonal wind fields from  
530 NAVGEM high-altitude analyses to clearly identify possible sources of any  
531 systematic errors is currently ongoing and will be the subject of a follow-on  
532 study.

#### 533 *4.2. Amplitude and phase of semi-diurnal, diurnal, and quasi-2 day features*

534 The results in Figures 4–18 together show that the vertical profiles of  
535  $U$  and  $V$  between 75–95 km during the two NH winter periods exhibit pe-  
536 riodic variations mainly at semi-diurnal, diurnal, and  $\sim 2$ -day periods. In  
537 this section, we examine the vertical profiles of  $S$ -transform amplitude and  
538 phase associated with these features to determine how well the high-altitude  
539 NAVGEM wind variations agree with the observed meteor radar wind vari-  
540 ations over the broad geographic range offered by the meteor radar sites. To  
541 do so, the  $S$ -transform was applied to time series of  $U$  and  $V$  between 75–95  
542 km altitude from each of the meteor radar sites over the time periods listed  
543 in Table 1 and to the corresponding NAVGEM  $U$  and  $V$  time series. Time  
544 averaged values of the amplitude  $|S|$  and phase  $\phi$  were computed from both  
545 NAVGEM and meteor radar winds at 2 cpd, 1 cpd, and 0.5 cpd using the  
546 scaling factor  $k=1$ . Standard deviations of the amplitude and phase about  
547 the time mean for each period were also computed at each of these frequen-  
548 cies in order to quantify the geophysical variability in the periodic features.  
549 The following sections present results from the first 8 sites listed in Table 1.  
550 Results for the ninth site, Rothera, are not presented since the  $S$ -transform  
551 analysis found very weak ( $<10 \text{ m s}^{-1}$ ) variations at these frequencies in both  
552 NAVGEM and radar winds.

##### 553 *4.2.1. Semi-diurnal variations*

554 Our analysis finds that the semi-diurnal (2 cpd) variations of  $U$  and  $V$   
555 during both 2009-2010 and 2012-2013 winters are strongest at the NH ex-  
556 tratropical stations of Andenes, Trondheim, Juliusruh, Collm, CMOR, and  
557 Bear Lake. Figures 19–24 plot the vertical profiles of the time averaged am-  
558 plitude and phase of the semi-diurnal component in  $U$  and  $V$  from these six  
559 stations. The error bars in these plots represent the standard deviation of  
560 the amplitude and phase about the time mean. The phase is expressed as  
561 local time of maximum wind.

562 The semi-diurnal amplitude and phase profiles in  $U$  and  $V$  at the high  
563 northern latitude locations of Andenes and Trondheim (Figs. 19 and 20)  
564 show very good qualitative and quantitative agreement overall between the

565 NAVGEM and meteor radar results. Exceptions to this agreement are found  
566 at Andenes (Fig. 19) where semi-diurnal amplitudes in NAVGEM  $V$  are con-  
567 sistentlly  $\sim 10 \text{ m s}^{-1}$  smaller than the meteor radar  $V$  amplitudes throughout  
568 the 75–95 km altitude range during December 2012 and February 2013, and  
569 also during January 2013 when the NAVGEM semi-diurnal  $U$  amplitudes are  
570 10–20  $\text{m s}^{-1}$  larger than the meteor radar  $U$  amplitudes. There is also dis-  
571 agreement between the NAVGEM and radar wind semi-diurnal  $U$  and  $V$  am-  
572 plitudes at Trondheim (Fig. 20) during February 2013, when the NAVGEM  
573 amplitudes are 10–15  $\text{m s}^{-1}$  less than the meteor radar amplitudes between  
574 85–95 km.

575 Figures 21 and 22 compare the semi-diurnal amplitude and phase in  $U$  and  
576  $V$  from NAVGEM and meteor radar observations at the Northern European  
577 stations of Juliusruh and Collm, respectively, for the two NH winter periods.  
578 The peak amplitudes in both  $U$  and  $V$  at these two midlatitude stations  
579 are larger than at the two Scandinavian stations locations (Fig. 19 and 20).  
580 Again, we find good overall agreement between the vertical profiles of semi-  
581 diurnal amplitude and phase from the NAVGEM and meteor radar winds at  
582 these two locations, although we note that the NAVGEM amplitudes during  
583 most months are  $\sim 5\text{--}10 \text{ m s}^{-1}$  larger than the meteor radar amplitudes.  
584 The largest discrepancies are found during January 2013 when NAVGEM  $V$   
585 amplitudes at both Juliusruh and Collm exceed the meteor radar amplitudes  
586 by  $20 \text{ m s}^{-1}$  between 90–95 km.

587 Figures 23 and 24 compare the vertical profiles of the semi-diurnal ampli-  
588 tude and phase in NAVGEM and meteor radar  $U$  and  $V$  at the North Amer-  
589 ican CMOR and Bear Lake sites, respectively. We find that the NAVGEM  
590 semi-diurnal amplitudes at CMOR (Fig. 23) are consistently  $10\text{--}20 \text{ m s}^{-1}$   
591 larger than the meteor radar amplitudes during all months. There is better  
592 agreement between the NAVGEM and meteor radar semi-diurnal amplitudes  
593 in  $U$  and  $V$  at Bear Lake (Fig. 24). At both of these locations, the phase  
594 profiles are in agreement. However, the standard deviations of the time av-  
595 eraged phase values are large compared to the northern European stations.  
596 These larger standard deviations suggest a non-stationary semi-diurnal signal  
597 in local time at these locations, particularly in the meridional wind profiles.

598 Figure 25 plots time averaged vertical profiles of semi-diurnal amplitude  
599 and phase at Ascension Island for the January–March 2010 period. There is  
600 good overall agreement between the NAVGEM and meteor radar amplitudes  
601 in  $U$  and  $V$ , with the exception of March 2010 when NAVGEM  $V$  amplitudes  
602 above 90 km are significantly larger than the meteor radar observations in-

603 dicare. At altitudes where the time averaged semi-diurnal amplitudes are  
604 relatively large ( $\sim 10\text{--}20\text{ m s}^{-1}$ ), there is good agreement between the semi-  
605 diurnal phases derived from the NAVGEM and meteor radar winds.

#### 606 *4.2.2. Diurnal variations*

607 Our analysis finds robust diurnal variations in horizontal winds at Ascen-  
608 sion Island during the January–March 2010 period and at Tierra del Fuego  
609 during the months of December 2012, February 2013, and March 2013. Fig-  
610 ure 26 plots time averaged profiles of diurnal (1 cpd) amplitude  $|S|$  and phase  
611  $\phi$  in  $U$  and  $V$  at both of these locations. At Ascension Island (left three  
612 columns in Fig. 26), the meteor radar observations show the largest diurnal  
613 variations in  $V$  ( $\sim 40\text{--}45\text{ m s}^{-1}$ ) during February and March 2010. Diurnal  
614 variations in NAVGEM  $V$  are exhibit good agreement with the radar esti-  
615 mates in January 2010 when diurnal amplitudes are smaller; during February  
616 and March 2010 the NAVGEM estimates are  $10\text{--}20\text{ m s}^{-1}$  larger than the  
617 radar-based values between  $75\text{--}88\text{ km}$ , and are  $\sim 10\text{ m s}^{-1}$  smaller than radar  
618 estimates above  $90\text{ km}$ . Both NAVGEM analyses and radar observation at  
619 Ascension Island show somewhat weaker diurnal variations in  $U$  during the  
620 January–March 2010 period, with peak values of  $20\text{--}30\text{ m s}^{-1}$ . Profiles of  
621 diurnal phase in  $U$  and  $V$  at this location exhibit good agreement.

622 Profiles of diurnal amplitude and phase in  $U$  and  $V$  at Tierra del Feugo  
623 from the radar winds and NAVGEM analyses are plotted in the right three  
624 columns of Figure 26. At this higher southern latitude ( $53^\circ\text{S}$ ), peak diurnal  
625 amplitudes are smaller ( $\sim 10\text{--}15\text{ m s}^{-1}$ ) than at Ascension Island ( $8^\circ\text{S}$ ). Cer-  
626 tain months show relatively poor agreement between the diurnal phase in the  
627 radar and NAVGEM winds, e.g., March 2013 for  $V$  and February 2013 for  
628  $U$ . For these months, the amplitude of the diurnal variation in  $U$  and  $V$  are  
629 very small ( $\sim 5\text{ m s}^{-1}$ ), making it difficult to isolate the phase as evidenced by  
630 the relatively large standard deviations in both radar and NAVGEM phase  
631 estimates.

#### 632 *4.2.3. Quasi-2 day variations*

633 The  $S$ -transform analysis finds variations in  $V$  at frequencies near  $0.5$   
634 cpd over Ascension Island during the January–March 2010 period. The  
635 quasi-2 day wave is a dominant feature of SH summer MLT winds that typi-  
636 cally exhibits peak amplitudes over a range of frequencies between  $0.45\text{--}0.6$   
637 cpd shortly after solstice (see, e.g. McCormack et al., 2010, and references  
638 therein). Our analysis finds that peak amplitudes in  $V$  of  $30\text{ m s}^{-1}$  occur at

639 0.52 cpd, and are comparable to the amplitude of the diurnal variations in  
640  $V$  seen at Ascension Island (Fig. 26). To illustrate this feature, Figure 27  
641 plots vertical profiles of the time-averaged amplitude and phase at 0.52 cpd  
642 in both  $U$  and  $V$  from the Ascension Island observations and NAVGEM anal-  
643 yses. There is good qualitative agreement in the amplitude and phase of the  
644 quasi-2 day signal in  $U$  and  $V$  from the radar and NAVGEM winds, although  
645 the NAVGEM results consistently underestimate the peak amplitudes in  $V$   
646 during February 2010 by  $\sim 10 \text{ m s}^{-1}$  relative to the radar winds.

#### 647 *4.3. Time dependence of periodic features during 2010 and 2013 SSWs*

648 In this section, we apply the  $S$ -transform to time series of  $U$  and  $V$  from  
649 both meteor radar observations and NAVGEM analyses to characterize the  
650 temporal variability of the semi-diurnal, diurnal, and quasi-2 day features  
651 discussed in the previous section. We focus in particular on time periods  
652 centered on the occurrence of SSWs in January 2010 and 2013 to determine  
653 how these features evolve during such large-scale changes in middle atmo-  
654 spheric circulation. We analyze NAVGEM and radar winds at the Juliusruh,  
655 Collm, Bear Lake, and CMOR locations during the periods from 15 January  
656 to 15 February 2010 and 25 December 2012 to 25 January 2013. In addition,  
657 we also examine winds at Ascension Island from 15 January to 15 February  
658 2010, and winds at Trondheim from December 25 2012 to January 25 2013.  
659 For this discussion, we limit our comparisons to the 87–88 km altitude range.  
660 This altitude range is chosen for several reasons: first, there are ample me-  
661 teor radar observations during these two time periods at this level; second,  
662 NAVGEM analyses in this region assimilate both MLS and SABER tem-  
663 perature profiles; third, NAVGEM results at this level should avoid possible  
664 influences of the imposed diffusion at the model upper boundary.

665 Figures 28, 29, 30, and 31 plot values of  $|S|$  as a function of time and  
666 frequency from NAVGEM and radar  $U$  and  $V$  at Juliusruh (88 km altitude),  
667 Collm (88 km), CMOR (88 km), and Bear Lake (87 km), respectively. In each  
668 of these figures, the vertical red lines denote the beginning of the NAVGEM  
669 mesospheric wind reversals on 27 January 2010 and 7 January 2013 associated  
670 with the onset of each SSW period, as discussed in Section 2 and illustrated  
671 in Fig. 1. The frequency range of these plots extends to 4 cpd, which is the  
672 Nyquist frequency for the 3-hourly NAVGEM output.

673 Figure 28a and 28b plot the time variations in  $|S|$  derived from NAVGEM  
674  $V$  and  $U$ , respectively, at Juliusruh during the January 2010 SSW period.  
675 The main feature in both fields is a semi-diurnal variation whose amplitude

676 decreases starting around the time of the mesospheric wind reversal on 27  
677 January for a period of 3–4 days, then begins to increase until reaching peak  
678 amplitude 7–10 days following the initial wind mesospheric wind reversal.  
679 Similar behavior is also seen in the Juliusruh meteor radar winds (Fig. 28c  
680 and 28d). Both NAVGEM and meteor radar winds show peak semi-diurnal  
681 amplitudes in  $U$  and  $V$  of  $\sim 50 \text{ m s}^{-1}$ . Figure 28e and 28f show that semi-  
682 diurnal amplitudes in NAVGEM  $V$  and  $U$ , respectively, for the January 2013  
683 SSW period also decrease around the time of the mesospheric wind reversal  
684 beginning on 7 January 2013. In this case, however, semi-diurnal amplitudes  
685 take longer to increase compared to the January 2010 case. Peak amplitudes  
686 in  $U$  and  $V$  are seen 12–14 days after the onset of the mesospheric wind  
687 reversal. The meteor radar winds (Fig. 28g and 28h) also show this behavior.

688 Figure 29 plots similar results for the nearby Collm site, showing de-  
689 creases in the semi-diurnal amplitudes around the time of the mesospheric  
690 wind reversal in both winters, followed by a relatively rapid increase in early  
691 February 2010 and a more gradual increase in mid-January 2013. We note  
692 that for both Juliusruh and Collm the peak NAVGEM amplitudes in mid-  
693 January 2013 are  $\sim 10\text{--}20 \text{ m s}^{-1}$  larger than the corresponding peak radar  
694 wind amplitudes. This is consistent with the larger time averaged semi-  
695 diurnal amplitudes in NAVGEM  $U$  and  $V$  compared to the meteor radar  
696 results seen in January 2013 in both Figs. 21 and 22.

697 Figures 30 and 31 plot the temporal evolution of the periodic features in  
698 NAVGEM and meteor radar  $U$  and  $V$  fields during the January 2010 and  
699 January 2013 SSW periods at the CMOR and Bear Lake sites, respectively.  
700 At these locations ( $42^\circ\text{--}43^\circ\text{N}$  latitude), semi-diurnal variations are again the  
701 dominant feature, although the amplitudes of these variations are generally  
702 smaller than at Juliusruh and Collm ( $51^\circ\text{--}54^\circ\text{N}$ ). During the January 2010  
703 event, the  $U$  and  $V$  fields from both NAVGEM analyses and radar observa-  
704 tions at CMOR and Bear Lake show semi-diurnal peaks on 23–24 January  
705 and 5–7 February. However, there is no clear decrease in semi-diurnal ampli-  
706 tudes around the time of the mesospheric wind reversal on 27 January as was  
707 seen at Juliusruh and Collm. During the January 2013 event, the NAVGEM  
708 and radar winds at both CMOR and Bear Lake exhibit peaks between 15–22  
709 January, which is consistent with the behavior observed at Juliusruh and  
710 Collm (Figs. 28 and 29, panels e–h). In contrast to the Juliusruh and Collm  
711 results, the semi-diurnal variability at CMOR and Bear Lake does not show  
712 a decrease in amplitude around the time of the mesospheric wind reversal on  
713 7 January; instead the NAVGEM and meteor radar winds show consistently

714 weak semi-diurnal amplitudes in both  $U$  and  $V$  throughout late December  
715 2012 and the first half of January 2013.

716 Figure 32 plots the  $S$ -transform results for NAVGEM and radar winds  
717 at 87 km over Trondheim during the January 2013 SSW event. The semi-  
718 diurnal variations at this high-latitude location ( $63^\circ\text{N}$ ) are similar to those  
719 seen at the lower-latitude locations, particularly the peak amplitudes in both  
720  $U$  and  $V$  occurring over the 15–22 January time frame. Overall there is  
721 good agreement between the semi-diurnal amplitudes from the NAVGEM  
722 and meteor radar winds during January 2013.

723 Figure 33 plots the  $S$ -transform results for Ascension Island ( $8^\circ\text{N}$ ) during  
724 the January 2010 SSW period from the NAVGEM analyses and radar winds  
725 at 88 km. To better highlight the lower-frequency variability, the frequency  
726 range in these plots is limited to 3 cpd. Prior to the stratospheric wind  
727 reversal, both NAVGEM and meteor radar  $V$  fields exhibit peaks at 1 cpd  
728 and 0.5 cpd. Beginning on 31 January, there is a rapid increase in amplitude  
729 near 0.5 cpd that is accompanied by a reduction in diurnal amplitudes. This  
730 amplification of the quasi-2 day wave in the Southern Hemisphere summer  
731 MLT around the time of a major SSW in NH winter is consistent with ear-  
732 lier studies of the quasi-2 day wave during January 2006 and January 2010  
733 (McCormack et al., 2009, 2010). In contrast to the  $V$  results, the NAVGEM  
734 and meteor radar  $U$  results at Ascension Island show comparatively mod-  
735 est variations in diurnal amplitudes throughout January 2013 and no strong  
736 quasi-2 day variations.

## 737 5. Discussion

738 The results presented in the previous section demonstrate that the 3-  
739 hourly output from the high-altitude NAVGEM forecast-analysis system ac-  
740 curately captures many of the key features in the meteor radar wind observa-  
741 tions over the 2009–2010 and 2012–2013 NH winter periods. These features  
742 include the altitude dependence of the time averaged amplitude and phase  
743 of the semi-diurnal tide in zonal and meridional winds, and the time evolu-  
744 tion of the main periodic features at semi-diurnal, diurnal, and quasi-2 day  
745 frequencies around the time of the SSWs in the two winters.

746 As discussed in the Introduction, several recent whole atmosphere mod-  
747 eling studies indicate that the migrating semi-diurnal tide is amplified in  
748 the NH extratropical MLT region following a major SSW event. Because  
749 these studies typically focus on one particular SSW event, it is difficult to

750 generalize their results to all SSWs. As Figure 1 illustrates, the timing and  
751 structure of the major SSWs in January 2010 and January 2013 are quite  
752 different, particularly with respect to the evolution and descent of easterly  
753 flow at high Northern latitudes from the mesosphere to the mid-stratosphere.  
754 These differences extend to the behavior of the semi-diurnal variation in  $U$   
755 and  $V$  following the 2010 and 2013 SSWs seen in Figs. 29–31.

756 With the understanding that no two SSWs will produce exactly the same  
757 MLT response, it is still useful to establish a generalized picture of how  
758 these events may influence tidal motions that can in turn impact the ther-  
759 mosphere/ionosphere system. To this end, a recent study by Limpasuvan  
760 et al. (2016) used a chemistry-climate model constrained by meteorologi-  
761 cal reanalyses below the 50 km level to examine the composite response of  
762 MLT dynamics to 13 SSW events between 1994 and 2012. A key finding of  
763 this study was that among the several different migrating and non-migrating  
764 tidal components examined, only the migrating semi-diurnal (SW2) ampli-  
765 tudes in the NH extratropics exhibited a robust response to the onset of a  
766 major SSW. Specifically, this study found an average amplification of  $\sim 3$  m  
767  $s^{-1}$  in SW2 amplitudes over the latitude range  $20^{\circ}\text{N}$ – $60^{\circ}\text{N}$  near 80 km alti-  
768 tude that increased to  $\sim 8$ – $10$  m  $s^{-1}$  at 100 km. The largest SW2 responses  
769 were found to occur 10–20 days following the onset of what was defined in  
770 Limpasuvan et al. (2016) to be an elevated-stratopause stratospheric sudden  
771 warming event (ES-SSW), which requires a zonal wind reversal at 1 hPa,  
772 a polar cap temperature below 190 K between 80–100 km, and a 10 km  
773 altitude discontinuity in stratopause height at high Northern latitudes.

774 To determine whether a similar type of response is evident in the high-  
775 altitude NAVGEM analyses of the January 2010 and January 2013 events,  
776 we computed mean semi-diurnal amplitude time series obtained from  $S$ -  
777 transform analysis of both NAVGEM and radar winds at altitudes between  
778 80–90 km using all NH radar locations with a continuous 30-day period of  
779 observations around the times of the 27 January 2010 and 7 January 2013  
780 mesospheric wind reversals. For the 2010 case, these locations are Juliusruh,  
781 Collm, CMOR, and Bear Lake. For the 2012–2013 case, these locations in-  
782 clude Juliusruh, Collm, CMOR, Bear Lake, and Trondheim. Figure 34 plots  
783 mean amplitudes of the semi-diurnal variation in  $V$  derived from NAVGEM  
784 analyses and radar observations from 15 January – 15 February 2010 (left  
785 column) and from 25 December 2012 – 25 January 2013 (right column). Ver-  
786 tical red lines in Fig. 34 indicate the dates of the mesospheric wind reversals  
787 in each year (see also Fig. 1).

788 In the 2010 case (Fig. 34, left column) both NAVGEM and radar wind ob-  
789 servations indicate a mean increase in semi-diurnal  $V$  amplitudes that begins  
790  $\sim 4$ –5 days after the wind reversal and peaks 10 days later. The NAVGEM  
791 results averaged among the four station locations show peak a semi-diurnal  
792 amplitude of  $51 \text{ m s}^{-1}$  between at 90 km, while the corresponding peak semi-  
793 diurnal amplitude from the radar wind data is  $54 \text{ m s}^{-1}$ . In the 2012/2013  
794 case (Fig. 34, right column), the mean NAVGEM and radar semi-diurnal  
795  $V$  amplitudes both exhibit a double peak structure between 85–90 km with  
796 two maxima on 17 January and 21 January, which occurs 10–14 days follow-  
797 ing the mesospheric wind reversal. For the January 2013 event, the mean  
798 NAVGEM results have a peak semi-diurnal amplitude of  $70 \text{ m s}^{-1}$  at 90 km  
799 on January 17, while the corresponding peak mean radar amplitude is only  
800  $50 \text{ m s}^{-1}$ .

801 Overall, the results in Fig. 34 indicate that the NAVGEM analyses cap-  
802 ture the qualitative nature of the mean response of the semi-diurnal variation  
803 in meridional winds between 80–90 km altitude obtained from the available  
804 NH meteor radar observations for the January 2010 and 2013 SSW events. In  
805 particular, both data sets show very similar behavior consisting of a peak in  
806 semi-diurnal  $V$  amplitudes 2–3 days prior to the mesospheric wind reversal,  
807 then a decrease in amplitude shortly after the reversal, followed by a steady  
808 increase in amplitude that peaks 10–14 days following the reversal. There  
809 are large discrepancies in the 2012/2013 case, where NAVGEM overestimates  
810 the peak semi-diurnal amplitudes from the radar observations by  $20 \text{ m s}^{-1}$  at  
811 90 km. Overestimation of the NAVGEM semi-diurnal amplitudes in both  $V$   
812 and  $U$  were also noted in the time averaged profiles at the Juliusruh, Collm,  
813 and CMOR sites during January 2013 (see Figs. 21, 22, and 23). The exact  
814 cause (or causes) of these quantitative discrepancies is not known at this  
815 time and is the subject of ongoing investigations. Here we discuss several  
816 possible factors that could affect the representation of the semi-diurnal tides  
817 and other dominant periodic motions in the current high-altitude NAVGEM  
818 analyzed winds.

819 First, we note that in the 25 December 2012 – 25 January 2013 case (Fig.  
820 34, right column), no SABER temperature profiles were available poleward  
821 of  $52^\circ\text{N}$  until after 7 January 2013, the date when the NAVGEM analyses in-  
822 dicate the onset of the mesospheric zonal wind reversal. Although changes in  
823 SABER coverage would be expected to mostly affect the NAVGEM analyses  
824 at high latitude locations such as Trondheim ( $63^\circ\text{N}$ ), and possibly midlati-  
825 tude locations near Collm and Juliusruh ( $51^\circ\text{N}$ – $54^\circ\text{N}$  latitude), it is not clear

826 at this time exactly how the changes in coverage would impact assimilation  
827 of the tides. Data denial experiments are needed to determine the exact lati-  
828 tude and time ranges over which the semi-diurnal feature (and other periodic  
829 variations) are affected by the introduction of SABER temperature profiles  
830 into the assimilation due to the satellite yaw cycle.

831 Second, differences in the semi-diurnal amplitudes extracted using the  
832 *S*-transform may arise due to the different temporal sampling, i.e., 3-hourly  
833 NAVGEM analysis/forecast winds versus hourly meteor radar wind observa-  
834 tions. The coarser NAVGEM time resolution might be expected to system-  
835 atically underestimate the semi-diurnal wind variations seen in the hourly  
836 radar winds. This does not seem to be the case in general, as there is good  
837 quantitative agreement between NAVGEM and radar wind estimates of the  
838 semi-diurnal amplitudes in most months throughout the 75–95 km region;  
839 there is no indication in Figs. 19–24 that the 3-hourly NAVGEM analy-  
840 ses systematically underestimate the semi-diurnal amplitudes relative to the  
841 radar wind results throughout the December – February period. However,  
842 several recent modeling studies have found that disturbed conditions in the  
843 MLT around the time of an SSW promote interactions between migrating  
844 tides, non-migrating tides, and planetary waves that can amplify a variety  
845 of tidal modes with frequencies at or near multiples of 0.5 cpd (e.g, Fuller-  
846 Rowell et al., 2010; Pedatella and Liu, 2013; Pedatella et al., 2014). It is  
847 possible that the 3-hourly NAVGEM output is not sufficient to isolate the  
848 semi-diurnal component among these other components around the time of  
849 an SSW, leading to discrepancies between estimates of the semi-diurnal am-  
850 plitude in winds from the high-altitude NAVGEM analysis and the meteor  
851 radar winds. To investigate this issue further, we plan to compare meteor  
852 radar observations with NAVGEM analyzed winds supplemented with 1-  
853 hourly NAVGEM forecast model output in a future study. In addition, we  
854 also plan to perform spatial filtering of the global NAVGEM analyzed winds  
855 to better isolate the migrating tides, e.g. the zonal wavenumber 1 diurnal  
856 tide, zonal wavenumber 2 semi-diurnal tide, etc., which can then be eval-  
857 uated through comparison with whole atmosphere model estimates of tidal  
858 behavior during SSW events.

859 Third, the representation of the tides in the high-altitude NAVGEM anal-  
860 yses could be affected by biases introduced into the system by the atmo-  
861 spheric forecast model component due to missing or incomplete treatments  
862 of key physical processes in the MLT. Because there are relatively few sources  
863 of observations in the MLT compared to the troposphere and lower strato-

864 sphere, the NAVGEM data assimilation algorithm relies heavily on the sys-  
865 tem’s forecast model component in the data-poor upper levels (i.e., 50–100  
866 km altitude) to produce an accurate background state that effectively fills  
867 in the gaps between observations. If the background state produced by the  
868 model produces a systematic bias relative to the observations over the 6-hour  
869 assimilation window, this can degrade performance and, in extreme cases,  
870 cause valid observations to be excluded from the analysis. The main areas  
871 where the current high-altitude NAVGEM forecast model can be improved  
872 to eliminate potential sources of bias are the treatment of GWD, the param-  
873 eterization of odd-oxygen photochemistry, and the description of exothermic  
874 chemical heating and non-local thermodynamic equilibrium (non-LTE) ef-  
875 fects that affect the energy budget of the atmospheric region above 90 km.  
876 Here we discuss each of these areas in more detail.

877 The GWD parameterization of Eckermann (2011), specifies tropospheric  
878 sources of momentum flux using empirically-derived analytic functions that  
879 may not, in certain cases, accurately capture GW sources related to the  
880 “flow of the day”. To address this issue, alternative approaches in which  
881 GW sources are more closely tied to the model’s tropospheric flow are under  
882 investigation. The ultimate goal of this work is to produce a physically-based  
883 description of GW momentum flux sources that produces the most realistic  
884 flow in the MLT region, thereby minimizing forecast model bias that could  
885 degrade the quality of the analyzed winds.

886 Currently, NAVGEM only assimilates ozone profiles up to the 0.6 hPa  
887 level ( $\sim 55$  km altitude), and relaxes the prognostic ozone fields back to a  
888 monthly zonal mean climatology above this level (Eckermann et al., 2009).  
889 This is necessary due to the fact that the model’s ozone photochemistry  
890 parameterization (McCormack et al., 2008) was originally designed for the  
891 stratosphere and does not account for diurnal ozone variations that become  
892 relatively large in the mesosphere. Given the established role that ozone  
893 heating plays in determining the temperature structure throughout the mid-  
894 dle atmosphere, and in light of recent results suggesting that modifications  
895 in stratospheric ozone heating can contribute to SW2 variations around the  
896 time of major SSWs (e.g. Goncharenko et al., 2012; Limpasuvan et al., 2016),  
897 efforts are underway to implement a comprehensive parameterization of odd-  
898 oxygen photochemistry valid from 10–100 km altitude.

899 Finally, the effects of exothermic chemical heating via, e.g., collisional de-  
900 activation and chemical recombination of atomic oxygen and non-LTE cool-  
901 ing to space by  $\text{CO}_2$  have not yet been incorporated into the high-altitude

902 NAVGEM forecast model. Future investigations will examine the impact  
903 of these processes on both short-term (0–6 hour) and longer term (0–5 day)  
904 forecasts in the MLT in an effort to reduce model bias and improve the upper  
905 level temperature and wind analyses.

906 While the above discussion identifies several areas for improvement in the  
907 high-altitude NAVGEM forecast model, it should be emphasized here that  
908 the initial comparisons between NAVGEM MLT winds and meteor radar ob-  
909 servations show very good overall agreement. This indicates that current fore-  
910 cast model performance is sufficient to generate accurate analysis/forecast  
911 fields within the 6-hour assimilation window, and that additional research  
912 devoted to improving overall system performance in the MLT is warranted.

## 913 **6. Summary**

914 This study of MLT winds produced with a new high-altitude forecast/assimilation  
915 system shows, for the first time, that global meteorological analyses ex-  
916 tending from the surface to  $\sim 100$  km based on assimilation of middle at-  
917 mospheric temperature and constituent observations can accurately repro-  
918 duce observed diurnal, semi-diurnal, and quasi-2 day variations in horizon-  
919 tal winds. Through detailed comparisons with meteor radar wind observa-  
920 tions from nine different sites ranging in latitude from  $69^\circ\text{N}$  to  $67^\circ\text{S}$  over  
921 two NH winter periods (2009–2010 and 2012–2013), we find that, overall,  
922 high-altitude NAVGEM analyzed winds capture the observed time-averaged  
923 vertical structure in both zonal and meridional winds in the MLT between  
924 75–90 km altitude. Furthermore, the NAVGEM analyses also accurately re-  
925 produce the observed time-averaged vertical profiles of both amplitude and  
926 phase associated with these periodic features in zonal and meridional wind.

927 The occurrence of major SSWs in January 2010 and January 2013 pro-  
928 vide an opportunity evaluate how well the NAVGEM MLT winds capture ob-  
929 served changes in semi-diurnal amplitude during periods when the dynamics  
930 of the middle atmosphere are highly disturbed. We find that both NAVGEM  
931 analyses and meteor wind observations indicate a decrease in semi-diurnal  
932 amplitudes over the NH extratropics for several days beginning around the  
933 time of the mesospheric wind reversals at  $60^\circ\text{N}$  that precede the major SSW  
934 event. This is followed by an increase in semi-diurnal wind amplitudes which  
935 peaks 10–14 days following the onset of mesospheric wind reversals.

936 The results of this initial validation study are encouraging, and support  
937 additional efforts to improve high-altitude data assimilation products that

938 can be used to constrain whole atmosphere models. These results also high-  
939 light the fact that continued high-quality MLT wind observations provided  
940 from a global network of meteor radars are critical for validation of future  
941 high-altitude specification and modeling efforts. Continued validation studies  
942 that employ direct MLT wind observations, high-altitude data assimilation  
943 products, and whole atmosphere modeling are needed to further improve  
944 our understanding of how variability in the lower atmosphere impacts the  
945 thermosphere/ionosphere system.

## 946 **7. Acknowledgments**

947 NAVGEM development was supported by the Chief of Naval Research.  
948 All NAVGEM simulations were performed under a grant of computer time  
949 from the Department of Defense High Performance Computing Moderniza-  
950 tion Program. Additional support for J. McCormack was provided by the  
951 NASA Heliophysics Division Living with a Star Program award NNH13AV95I.  
952 Support for R. de Wit was provided by the NASA Postdoctoral Program,  
953 administered by the Universities Space Research Association. Support for D.  
954 Fritts was provided the National Science Foundation grant AGS-1112830.

Table 1: Location, time coverage, and technical details of the meteor radar observations used for comparison with NAVGEM winds.  $F$  represents radar frequency in MHz,  $PRF$  represents the pulse repetition frequency in Hz,  $\Delta z$  is the vertical resolution of the retrieved horizontal wind profiles in km, and  $P$  is power in kW.

Station	Location	$F$ (MHz)	$PRF$ (Hz)	$\Delta z$ (km)	$P$ (kW)	Period	Reference
Andenes	69.3°N 16.0°E	32.55	2094	2	30	1–18 Dec 2009,1–26 Jan,12–28 Feb 2010 1–20 Dec 2012,1–28 Jan,1–24 Feb 2013	Stober et al. (2012)
Trondheim	63.4°N 10.5°E	34.21	925	2	30	1 Dec 2012 – 28 Feb 2013	de Wit et al. (2015)
Juliusruh (dual)	54.6°N13.4°E	32.5/53.5	2144	2	15/15	1 Dec 2009 – 28 Feb 2010 1 Dec 2012 – 28 Feb 2013	de Wit et al. (2015)
Collm	51.3°N 13.0°E	36.20	2144	2	6	1 Dec 2009 – 28 Feb 2010 1 Dec 2012 – 28 Feb 2013	Stober et al. (2012)
CMOR (dual)	43.3°N 80.0°W	29.85/38.15532		3	6/6	1 Dec 2009 – 28 Feb 2010 1 Dec 2012 – 26 Feb 2013	Webster et al. (2004)
Bear Lake	41.9°N 111.4°W	35.20	2144	2	12	1 Dec 2009 – 28 Feb 2010 1 Dec 2012 – 28 Feb 2013	Day et al. (2012)
Ascension Is.	8.0°S 14.4°W	43.5	2144	2	6	1 Jan 2010 – 31 Mar 2010	de Wit et al. (2013)
Tierra del Feugo	53.7°S 67.7°W	32.55	1765	2	60	1–31 Dec 2012,1 Feb–31 Mar 2013	Fritts et al. (2010b)
Rothera	67.5°S 68.0°W	32.50	2144	2	6	15 Jan 2013 – 28 Feb 2013	Sandford et al. (2010)

955 **References**

- 956 Akmaev, R.A., 2011. Whole atmosphere modeling: Connecting terrestrial  
957 and space weather. *Rev. Geophys.* 49. doi:10.1029/2011RG000364.
- 958 Anderson, D., Araujo-Pradere, E.A., 2010. Sudden stratospheric warming  
959 event signatures in daytime E x B drift velocities in the Peruvian and  
960 Philippine longitude sectors for January 2003 and 2004. *J. Geophys. Res.*  
961 115. doi:10.1029/2010JA015337.
- 962 Baron, P., Murtaugh, D., Urban, J., Sagawa, H., Ochiai, S., Kasai, Y.,  
963 Kikuchi, K., Khosrawi, F., Körnich, H., Mizobuchi, S., Sagi, K., Yasui,  
964 M., 2013. Observation of horizontal winds in the middle-atmosphere be-  
965 tween 30°S and 55°N during the northern winter 2009–2010. *Atmos. Chem.*  
966 *Phys.* 13, 60496064. doi:10.5194/acp-13-6049-2013.
- 967 Bell, W., English, S.J., Candy, B., Atkinson, N., Hilton, F., Baker,  
968 N., Swadley, S.D., Campbell, W.F., Bormann, N., Kelly, G., Kazu-  
969 mori, M., 2008. The assimilation of SSMIS radiances in numerical  
970 weather prediction models. *IEEE Trans. Geosci. Remote Sens.* 46.  
971 doi:10.1109/TGRS.2008.917335.
- 972 Chau, J.L., Fejer, B.G., Goncharenko, L.P., 2009. Quiet variability of equa-  
973 torial E x B drifts during a sudden stratospheric warming event. *Geophys.*  
974 *Res. Lett.* 36. doi:10.1029/2008GL036785.
- 975 Day, K.A., Taylor, M.J., Mitchell, N.J., 2012. Mean winds, temperatures and  
976 the 16- and 5-day planetary waves in the mesosphere and lower thermo-  
977 sphere over Bear Lake Observatory (42°N, 111°W). *Atmos. Chem. Phys.*  
978 12, 1571–1585. doi:10.5194/acp-12-1571-2012.
- 979 Eckermann, S.D., 2011. Explicitly stochastic parameterization of  
980 nonorographic gravity-wave drag. *J. Atmos. Sci* 68, 1749–1765.  
981 doi:10.1175/2011JAS3684.1.
- 982 Eckermann, S.D., Hoppel, K.W., Coy, L., McCormack, J.P., Siskind, D.E.,  
983 Nielsen, K., Kochenash, A., Stevens, M.H., Englert, C.R., Singer, W.,  
984 Hervig, M., 2009. High-altitude data assimilation system experiments for  
985 the northern summer mesosphere season of 2007. *J. Atmos. Sol.-Terr.*  
986 *Phys.* 71, 531–551. doi:10.1016/j.jastp.2008.09.036.

- 987 Fritts, D.C., Janches, D., Hocking, W.K., 2010a. Southern Argentina Agile  
988 Meteor Radar: Initial assessment of gravity wave momentum fluxes. *J.*  
989 *Geophys. Res.* 115. doi:10.1029/2010JD013891.
- 990 Fritts, D.C., Janches, D., Iimura, H., Hocking, W.K., Mitchell, N.J., Stock-  
991 well, R.G., Fuller, B., Vandeppeer, B., Hormaechea, J., Brunini, C., Levato,  
992 H., 2010b. Southern Argentina Agile Meteor Radar: System design and  
993 initial measurements of largescale winds and tides. *J. Geophys. Res.* 115.  
994 doi:doi:10.1029/2010JD013850.
- 995 Fuller-Rowell, T., Wu, F., Akmaev, R., Fang, T., AraujoPradere, E., 2010. A  
996 whole atmosphere model simulation of the impact of a sudden stratospheric  
997 warming on thermosphere dynamics and electrodynamics. *J. Geophys. Res.*  
998 115. doi:10.1029/2010JA015524.
- 999 Goncharenko, L.P., Chau, J.L., Condor, P., Coster, A., Benkevitch, L., 2013a.  
1000 Ionospheric effects of sudden stratospheric warming during moderate-to-  
1001 high solar activity: Case study of January 2013. *Geophys. Res. Lett.* 40,  
1002 4982–4986. doi:10.1029/grl.50980.
- 1003 Goncharenko, L.P., Chau, J.L., Liu, H.L., Coster, A.J., 2010. Unexpected  
1004 connections between the stratosphere and ionosphere. *Geophys. Res. Lett.*  
1005 37. doi:10.1029/2010GL043125.
- 1006 Goncharenko, L.P., Coster, A.J., Plumb, R.A., Domeisen, D.I.V., 2012.  
1007 The potential role of stratospheric ozone in the stratosphere-ionosphere  
1008 coupling during stratospheric warmings. *Geophys. Res. Lett.* 39.  
1009 doi:10.1029/2012GL051261.
- 1010 Goncharenko, L.P., Hsu, V.W., Garnett, C., Brum, M., Zhang, S.R., Fentzke,  
1011 J.T., 2013b. Wave signatures in the midlatitude ionosphere during a sud-  
1012 den stratospheric warming of January 2010. *J. Geophys. Res.* 118, 472–487.  
1013 doi:10.1029/2012JA018251.
- 1014 Han, Y., van Delst, P., Weng, F., 2010. An improved fast radiative trans-  
1015 fer model for special sensor microwave imager/sounder upper atmosphere  
1016 sounding channels. *J. Geophys. Res.* 115. doi:10.1029/2010JD013878.
- 1017 Hocking, W., Fuller, B., Vandeppeer, B., 2001. Real-time determination of  
1018 meteor-related parameters utilizing modern digital technology. *J. Atm.*  
1019 *Sol-Terr. Phys.* 63, 155 – 169.

- 1020 Hogan, T., Liu, M., Ridout, J., Peng, M., Whitcomb, T., Ruston, B.,  
1021 Reynolds, C., Eckermann, S., Moskaitis, J., Baker, N., McCormack, J.,  
1022 Viner, K., McLay, J., Flatau, M., Xu, L., Chen, C., Chang, S., 2014.  
1023 The Navy Global Environmental Model. *Oceanography* 27, 116–125.  
1024 doi:10.5670/oceanog.2014.73.
- 1025 Hoppel, K.W., Eckermann, S.D., Coy, L., Nedoluha, G.E., Allen, D.R.,  
1026 Swadley, S.D., Baker, N.L., 2013. Evaluation of SSMIS upper atmosphere  
1027 sounding channels for high-altitude data assimilation. *Mon. Wea. Rev.*  
1028 141, 3314 – 3330. doi:10.1175/MWR-D-13-00003.1.
- 1029 Jin, H., Miyoshi, Y., Pancheva, D., Mukhtarov, P., Fujiwara, H., Shinagawa,  
1030 H., 2012. Response of migrating tides to the stratospheric sudden warming  
1031 in 2009 and their effects on the ionosphere studied by a whole atmosphere–  
1032 ionosphere model GAIA with COSMIC and TIMED/SABER observations.  
1033 *J. Geophys. Res.* 117. doi:10.1029/2012JA017650.
- 1034 Juang, H., 2011. A Multiconserving Discretization with Enthalpy as a Ther-  
1035 modynamic Prognostic Variable in Generalized Hybrid Vertical Coordi-  
1036 nates for the NCEP Global Forecast System. *Mon. Wea. Rev.* 139, 1583–  
1037 1607.
- 1038 Kuhl, D., Rosmond, T., Bishop, C., McLay, J., Baker, N., 2013. Comparison  
1039 of hybrid ensemble/4DVar and 4DVar within the NAVDAS-AR data assim-  
1040 ilation framework. *Mon. Wea. Rev.* 141, 2740–2758. doi:10.1175/MWR-  
1041 D-12-00182.1.
- 1042 Kuttippurath, J., Nikulin, G., 2012. A comparative study of the major  
1043 sudden stratospheric warmings in the Arctic winters 2003/20042009/2010.  
1044 *Atmos. Chem. Phys.* 12, 81158129. doi:10.5194/acp-12-8115-2012.
- 1045 Lieberman, R.S., Riggin, D.M., Siskind, D.E., 2013. Stationary waves  
1046 in the wintertime mesosphere: Evidence for gravity wave filtering  
1047 by stratospheric planetary waves. *J. Geophys. Res.* 118, 3129–3149.  
1048 doi:10.1002/jgrd.50319.
- 1049 Limpasuvan, V., Orsolini, Y.J., Chandran, A., Garcia, R.R., Smith, A.K.,  
1050 2016. On the composite response of the MLT to major sudden stratospheric  
1051 warming events with elevated stratopause. *J. Geophys. Res.* 121, 4518–  
1052 45376. doi:10.1002/2015JD024401.

- 1053 Limpasuvan, V., Wu, D.L., Schwartz, M.J., Waters, J.W., Wu, Q.,  
1054 Killeen, T.L., 2005. The two-day wave in EOS MLS temperature and  
1055 wind measurements during 2004–2005 winter. *Geophys. Res. Lett.* 32.  
1056 doi:10.1029/2005GL023396.
- 1057 Lin, J.T., Lin, C.H., Chang, L.C., Huang, H.H., Liu, J.Y., Chen, A.B., Chen,  
1058 C.H., Liu, C.H., 2012. Observational evidence of ionospheric migrating tide  
1059 modification during the 2009 stratospheric sudden warming. *Geophys. Res.*  
1060 *Lett.* 39. doi:10.1029/2011GL050248.
- 1061 Livesey, N., Read, W., Froidevaux, L., Lambert, A., Manney, G., Pumphrey,  
1062 H., Santee, M., Schwartz, M., Wang, S., Cofeld, R., Cuddy, D., Fuller, R.,  
1063 Jarnot, R., Jiang, J., Knosp, B., Stek, P., Wagner, P., Wu, D., 2011. Earth  
1064 Observing System (EOS) Aura Microwave Limb Sounder version 3.3 level  
1065 2 data quality and description document. Technical Report JPL D-33509.  
1066 Jet Propulsion Laboratory, California Institute of Technology. Pasadena,  
1067 California USA.
- 1068 Manney, G.L., Kruger, K., Pawson, S., Minschwaner, K., Schwartz, M.J.,  
1069 Daffer, W.H., Livesey, N.J., Remsberg, M.G.M.E.E., III, J.M.R., Waters,  
1070 J.W., 2008. The evolution of the stratopause during the 2006 major warm-  
1071 ing: Satellite data and assimilated meteorological analyses. *J. Geophys.*  
1072 *Res.* 113. doi:10.1029/2007JD009097.
- 1073 Matthias, V., Hoffmann, P., Manson, A., Meek, C., Stober, G., Brown,  
1074 P., Rapp, M., 2013. The impact of planetary waves on the latitudi-  
1075 nal displacement of sudden stratospheric warmings. *Annales Geophysicae* 31,  
1076 1397–1415. URL: <http://www.ann-geophys.net/31/1397/2013/>,  
1077 doi:10.5194/angeo-31-1397-2013.
- 1078 Matthias, V., Hoffmann, P., Rapp, M., Baumgarten, G., 2012. Com-  
1079 posite analysis of the temporal development of waves in the pol-  
1080 ar mlt region during stratospheric warmings. *Journal of At-*  
1081 *mospheric and Solar-Terrestrial Physics* 90 - 91, 86 – 96. URL:  
1082 <http://www.sciencedirect.com/science/article/pii/S1364682612001113>,  
1083 doi:<http://dx.doi.org/10.1016/j.jastp.2012.04.004>. recent Progress in the  
1084 Vertical Coupling in the Atmosphere-Ionosphere System.
- 1085 McCormack, J.P., Coy, L., Hoppel, K.W., 2009. Evolution of the

- 1086 quasi-2 day wave during January 2006. *J. Geophys. Res.* 114.  
1087 doi:10.1029/2009JD012239.
- 1088 McCormack, J.P., Coy, L., Singer, W., 2014. Intraseasonal and interannual  
1089 variability of the quasi 2 day wave in the northern hemisphere summer  
1090 mesosphere. *J. Geophys. Res.* 119, 2928–2946. doi:10.1002/2013JD020199.
- 1091 McCormack, J.P., Eckermann, S.D., Hoppel, K.W., Vincent, R.A.,  
1092 2010. Amplification of the quasi-two day wave through nonlinear in-  
1093 teraction with the migrating diurnal tide. *Geophys. Res. Lett.* 37.  
1094 doi:10.1029/2010GL043906.
- 1095 McCormack, J.P., Hoppel, K.W., Siskind, D.E., 2008. Parameterization of  
1096 middle atmospheric water vapor photochemistry for high-altitude NWP  
1097 and data assimilation. *Atmos. Chem. Phys.* 8, 7519–7532.
- 1098 McLandress, C.M., Scinocca, J.F., Shepherd, T.G., Reader, M.C., Man-  
1099 ney, G.L., 2013. Dynamical control of the mesosphere by orographic and  
1100 nonorographic gravity wave drag during the extended northern winters  
1101 of 2006 and 2009. *J. Atmos. Sci.* 70, 2152–2169. doi:10.1175/JAS-D-12-  
1102 0297.1.
- 1103 Niciejewski, R., Wu, Q., Skinner, W., Gell, D., Cooper, M., Marshall,  
1104 A., Killeen, T., Solomon, S., Ortland, D., 2006. Timed doppler in-  
1105 terferometer on the thermosphere ionosphere mesosphere energetics and  
1106 dynamics satellite: Data product overview. *J. Geophys. Res.* 111.  
1107 doi:10.1029/2005JA011513.
- 1108 Pedatella, N.M., Forbes, J.M., 2010. Evidence for stratospheric sudden  
1109 warming-ionosphere coupling due to vertically propagating tides. *Geo-  
1110 phys. Res. Lett.* 37. doi:10.1029/2010GL043560.
- 1111 Pedatella, N.M., Fuller-Rowell, T., Wang, H., Jin, H., Miyoshi, Y., Fuji-  
1112 wara, H., Shinagawa, H., , Liu, H.L., Sassi, F., Schmidt, H., Matthias,  
1113 V., Goncharenko, L., 2014. The neutral dynamics during the 2009 sudden  
1114 stratosphere warming simulated by different whole atmosphere models. *J.  
1115 Geophys. Res.* 119, 13061324. doi:10.1002/2013JA019421.
- 1116 Pedatella, N.M., Liu, H.L., 2013. The influence of atmospheric tide and plan-  
1117 etary wave variability during sudden stratosphere warmings on the low lati-  
1118 tude ionosphere. *J. Geophys. Res.* 118, 5333–5347. doi:10.1002/jgra.50492.

- 1119 Rezac, L., Jian, Y., Yue, J., III, J.M.R., Kutepov, A., Garcia, R., Walker,  
1120 K., Bernath, P., 2015. Validation of the global distribution of CO<sub>2</sub> volume  
1121 mixing ratio in the mesosphere and lower thermosphere from saber. *J.*  
1122 *Geophys. Res.* 120, 12,067–120,081. doi:10.1002/2015JD023955.
- 1123 Riggins, D., Meyer, C., Fritts, D., Jarvis, M., Murayama, Y., Singer, W., Vin-  
1124 cent, R., Murphy, D., 2003. MF radar observations of seasonal variability  
1125 of semidiurnal motions in the mesosphere at high northern and south-  
1126 ern latitudes. *J. Atm. Sol.-Terr. Phys* 65, 483–493. doi:10.1016/S1364-  
1127 6826(02)00340-1.
- 1128 Sandford, D.J., Beldon<sup>1</sup>, C.L., Hibbins<sup>2</sup>, R.E., Mitchell, N.J., 2010. Dynam-  
1129 ics of the Antarctic and Arctic mesosphere and lower thermosphere Part  
1130 1: Mean winds. *Atmos. Chem. Phys.* 10, 10273–10289. doi:10.5194/acp-  
1131 10-10273-2010.
- 1132 Sassi, F., Liu, H.L., 2014. Westward traveling planetary wave events  
1133 in the lower thermosphere during solar minimum conditions sim-  
1134 ulated by SD-WACCM-X. *J. Atm. Sol-Terr.,Phys.* 119, 11–26.  
1135 doi:10.1016/j.jastp.2014.06.009.
- 1136 Sassi, F., Liu, H.L., Ma, J., Garcia, R.R., 2013. The lower thermosphere  
1137 during the northern hemisphere winter of 2009: A modeling study using  
1138 high-altitude data assimilation products in WACCM-X. *J. Geophys. Res.*  
1139 118, 8954–8969. doi:10.1002/jgrd.50632.
- 1140 Siskind, D.E., Eckermann, S.D., McCormack, J.P., Coy, L., Hoppel, K.W.,  
1141 Baker, N.L., 2010. Case studies of the mesospheric response to recent  
1142 minor, major, and extended stratospheric warmings. *J. Geophys. Res.*  
1143 115. doi:10.1029/2010JD014114.
- 1144 Smolarkiewicz, P.K., Pudykiewicz, J., 1992. A class of semi-Lagrangian ap-  
1145 proximations for fluids. *J. Atmos. Sci.* 49, 2082–2096.
- 1146 Staniforth, A., White, A., Wood, N., Thuburn, J., Zerroukat, M., Cordero,  
1147 E., Davies, T., 2006. The Joy of U.M. 6.3- Model Formulation. Technical  
1148 Report 15. United Kingdom Meteorological Office. Met Office, FitzRoy  
1149 Road, Exeter, UK.

- 1150 Stober, G., Jacobi, C., Matthias, V., Hoffmann, P., Gerding, M., 2012.  
1151 Neutral air density variations during strong planetary wave activ-  
1152 ity in the mesopause region derived from meteor radar observations.  
1153 Journal of Atmospheric and Solar-Terrestrial Physics 74, 55 – 63. URL:  
1154 <http://www.sciencedirect.com/science/article/pii/S136468261100280X>,  
1155 doi:<http://dx.doi.org/10.1016/j.jastp.2011.10.007>.
- 1156 Stockwell, R.G., Mansinha, L., Lowe, R.P., 1996. Localization of the complex  
1157 spectrum: The S transform. IEEE Trans. Sig. Process. 44, 998–1001.
- 1158 Stray, N., Orsolini, Y.J., Espy, P.J., Limpasuvan, V., Hibbins, R.E., 2015.  
1159 Observations of planetary waves in the mesosphere-lower thermosphere  
1160 during stratospheric warming events. Atmos. Chem. Phys. 15, 4997–5005.  
1161 doi:10.5194/acp-15-4997-2015.
- 1162 Swadley, S., Poe, G., Bell, W., Hong, Y., Kunkee, D.B., McDermid, I.S.,  
1163 Leblanc, T., 2008. Analysis and characterization of the SSMIS Upper At-  
1164 mosphere Sounding Channel Measurements. IEEE Trans. Geosci. Remote  
1165 Sens. 46, 962–983. doi:10.1109/TGRS.2008.916980.
- 1166 Ventosa, S., Simon, C., Schimmel, M., Danobeitia, J.J., Manuel, A., 2008.  
1167 The S-Transform from a wavelet point of view. IEEE Trans. Signal Process.  
1168 56, 2771–2780. doi:10.1109/TSP.2008.917029.
- 1169 Wang, H., Fuller-Rowell, T.J., Akmaev, R.A., Hu, M., Kleist, D.T., Iredell,  
1170 M.D., 2011. First simulations with a whole atmosphere data assimila-  
1171 tion and forecast system: The January 2009 major sudden stratospheric  
1172 warming. J. Geophys. Res. 116. doi:10.1029/2011JA017081.
- 1173 Webster, A.R., Brown, P.G., Jones, J., Ellis, K.J., Campbell-Brown, M.,  
1174 2004. Canadian Meteor Orbit Radar (CMOR). Atmos. Chem. Phys. 4,  
1175 679–684.
- 1176 de Wit, R., Hibbins, R., Espy, P., 2015. The seasonal cycle of gravity  
1177 wave momentum flux and forcing in the high latitude northern hemisphere  
1178 mesopause region . J. Atmos. Sol.-Terr. Phys. 127, 21–29.
- 1179 de Wit, R.J., Hibbins, R.E., Espy, P.J., Mitchell, N.J., 2013. Interannual  
1180 variability of mesopause zonal winds over Ascension Island: Coupling to  
1181 the stratospheric QBO. J. Geophys. Res. 118, 12052–12060.

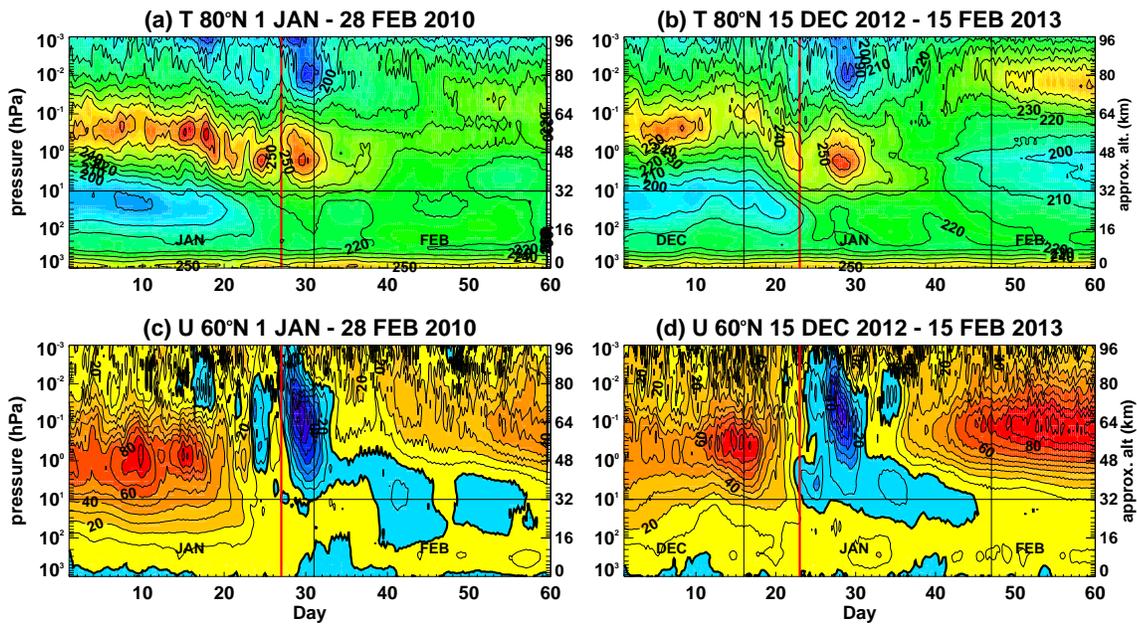


Figure 1: Altitude-time sections of zonal mean temperatures (a & b) and zonal mean zonal winds (c & d) from 6-hourly NAVGEM analyses for (a & c) 1 January – 28 February 2010 and (b & d) for 15 December 2012 – 15 February 2013. Values along the abscissa denote days from the beginning of each period. Red vertical lines denote dates of sustained mesospheric wind reversal at 60°N in each winter, i.e., 27 January 2010 and 7 January 2013, as described in the text. Contours are drawn every 10 K and 10  $m^{-1}$ . Bold contour in (c) and (d) denotes zero wind line.

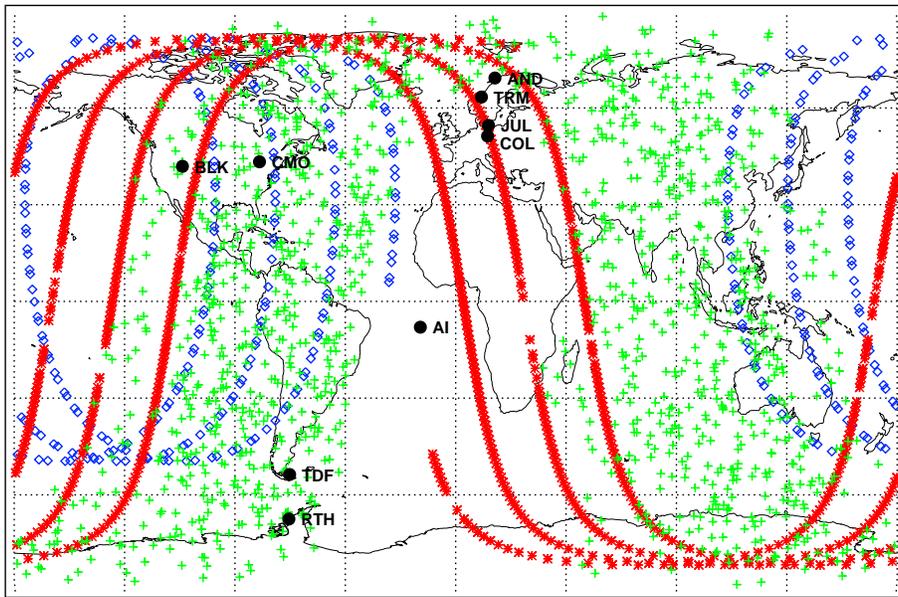


Figure 2: An example of the geographic coverage of SABER (blue), MLS (red), and UAS (green) observations for a single 6-hour NAVGEM analysis window centered on 12 UTC 30 January 2010. Black dots indicate locations of the nine meteor radar stations listed in Table 1.)

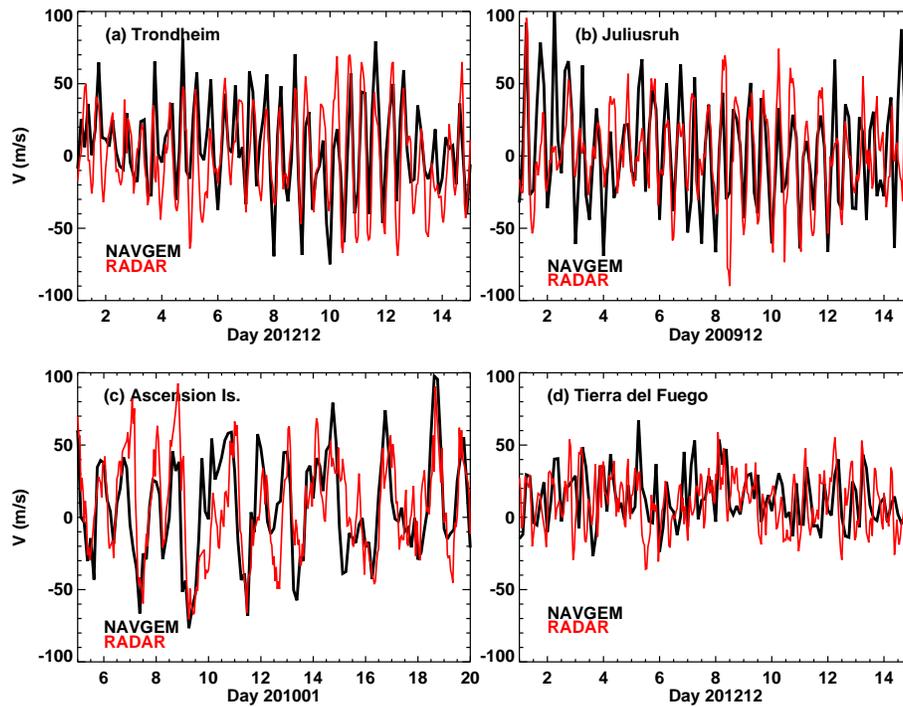


Figure 3: Time series of meridional wind from high-altitude NAVGEM (black) and from meteor radar observations (red) for (a) 1–15 December 2012 over Trondheim at 87 km, (b) 1–15 December 2009 over Juliusruh at 88 km altitude, (c) 5–20 January 2010 over Ascension Island at 87 km; (d) 1–15 December 2012 over Tierra del Fuego at 87 km.

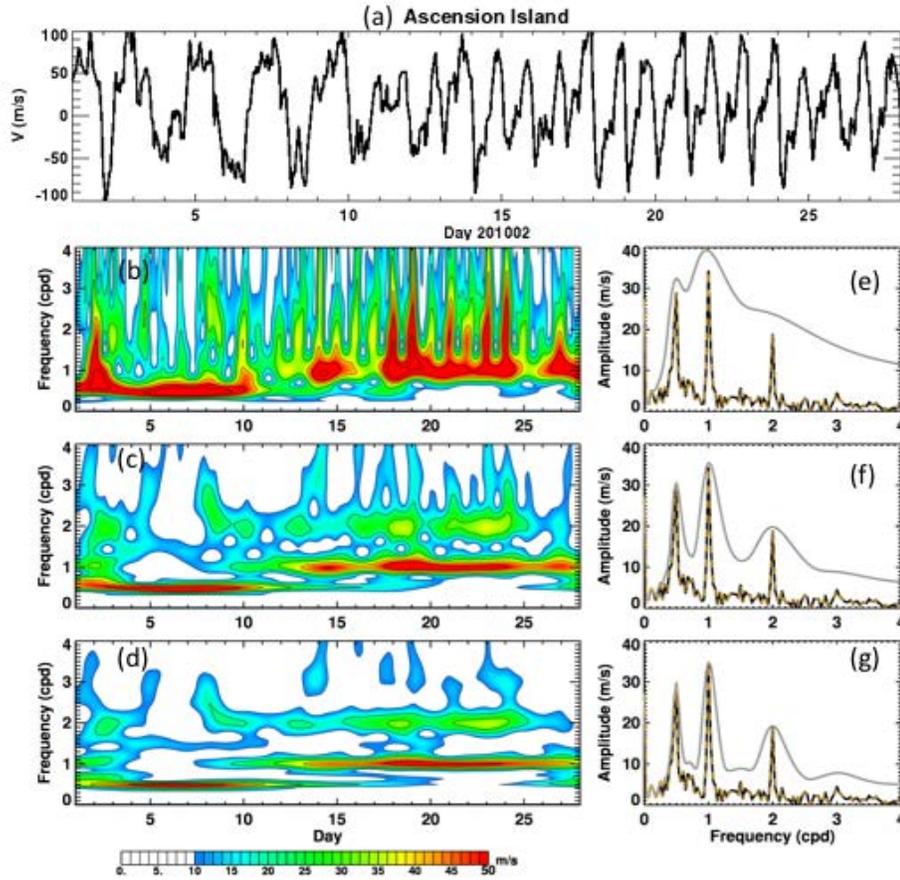


Figure 4: (a) Time series of hourly meridional winds at 87 km from the Ascension Island meteor radar over 1–28 February 2010. (Left column) Time-varying wave spectra of the 87 km winds obtained with the  $S$ -transform. (right column) Wave spectra obtained using a fast Fourier transform (black curves), time-integrated complex wave spectra  $\langle S \rangle$  (orange dashed curves), and monthly averages of the instantaneous amplitudes  $|S|$  (gray curves).  $S$ -transform results in (b) and (e) use a scaling factor of  $k = 0.5$ ; (c) and (f) use  $k = 1.0$ ; (d) and (g) use  $k = 1.5$ .

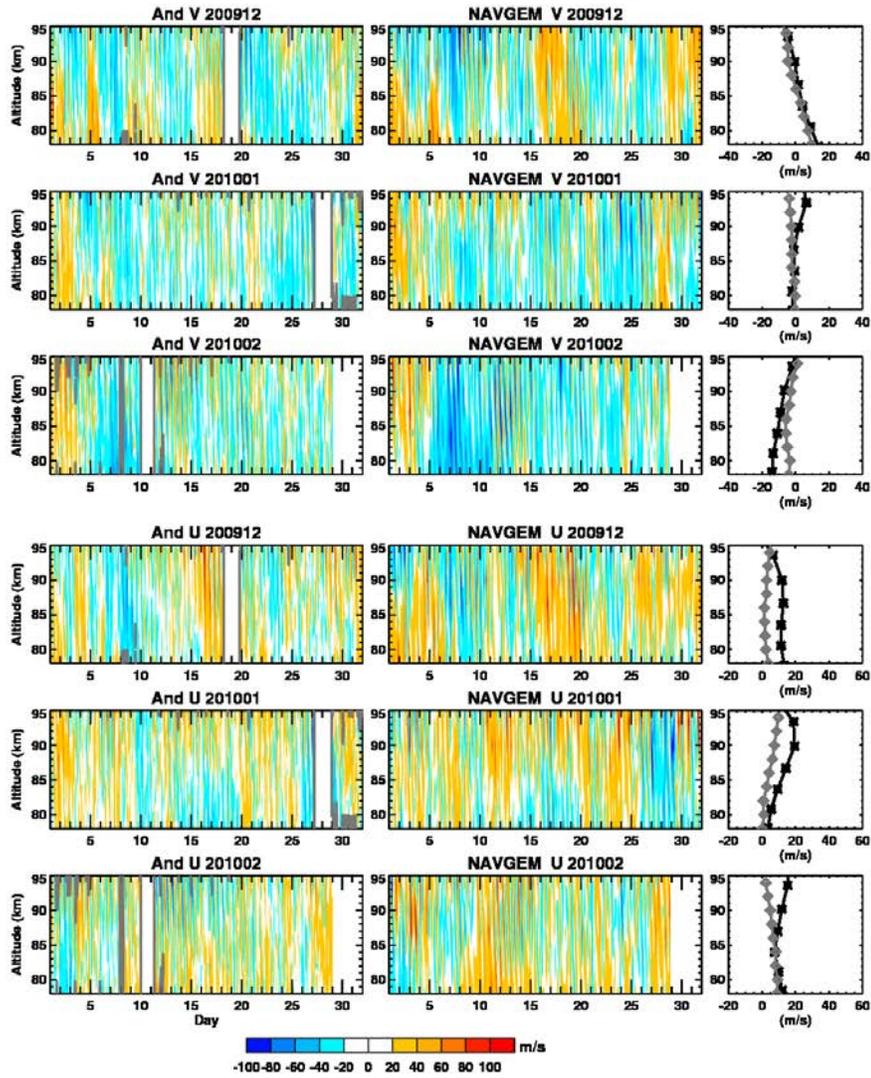


Figure 5: Meridional and zonal winds from meteor radar observations (left column) and NAVGEM analyses (center column) at Andenes for the 2009–2010 winter. Gray contours denote missing data. Corresponding monthly mean wind profiles (right column) from NAVGEM (black stars) and meteor radar observations (gray diamonds).

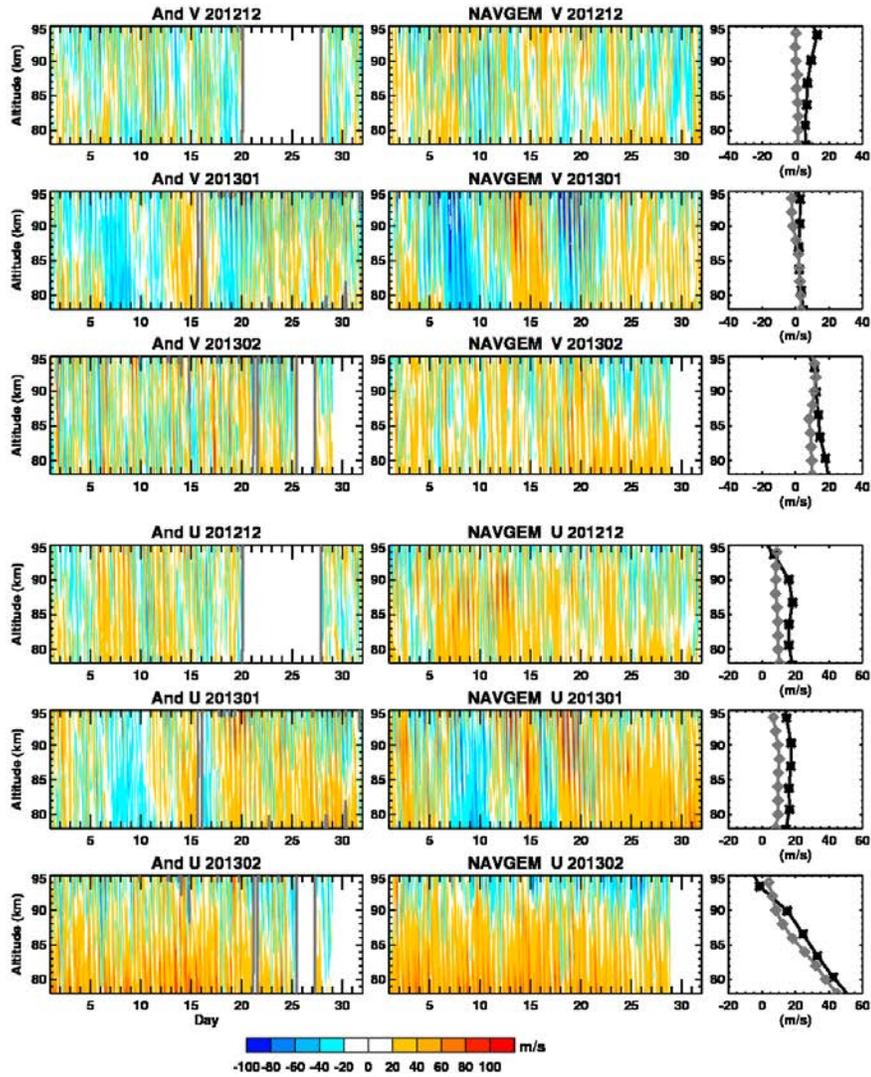


Figure 6: As in Figure 5 but for the 2012–2013 winter.

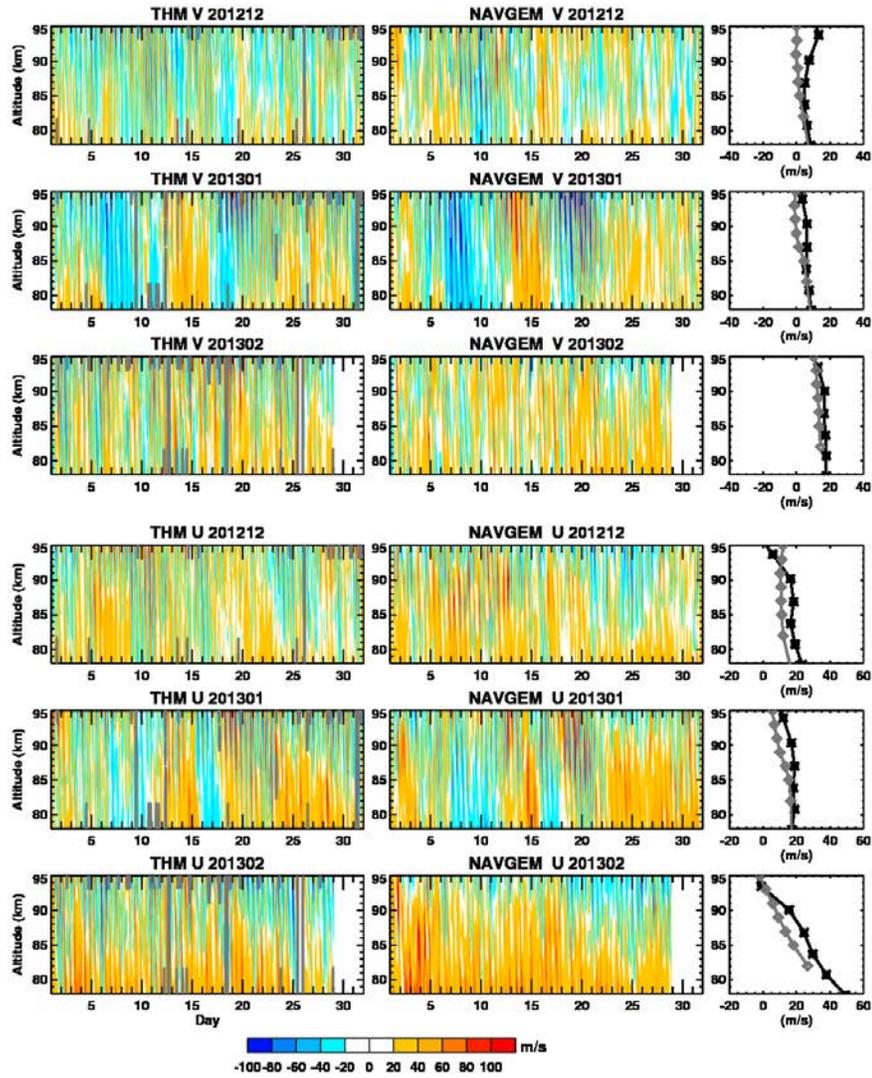


Figure 7: Meridional and zonal winds from meteor radar observations (left column) and NAVGEM analyses (center column) at Trondheim for the 2012–2013 winter. Gray contours denote missing data. Corresponding monthly mean wind profiles (right column) from NAVGEM (black stars) and meteor radar observations (gray diamonds).

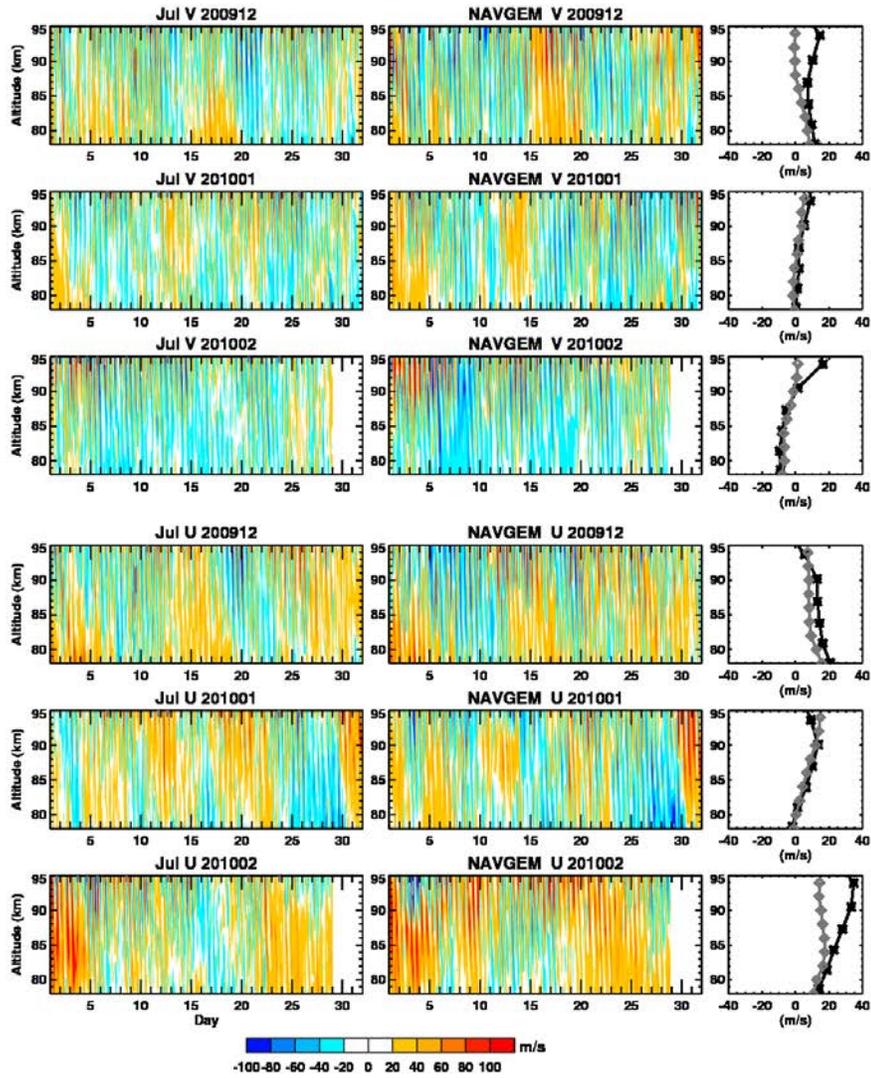


Figure 8: Meridional and zonal winds from meteor radar observations (left column) and NAVGEM analyses (center column) at Juliusruh for the 2009–2010 winter. Gray contours denote missing data. Corresponding monthly mean wind profiles (right column) from NAVGEM (black stars) and meteor radar observations (gray diamonds).

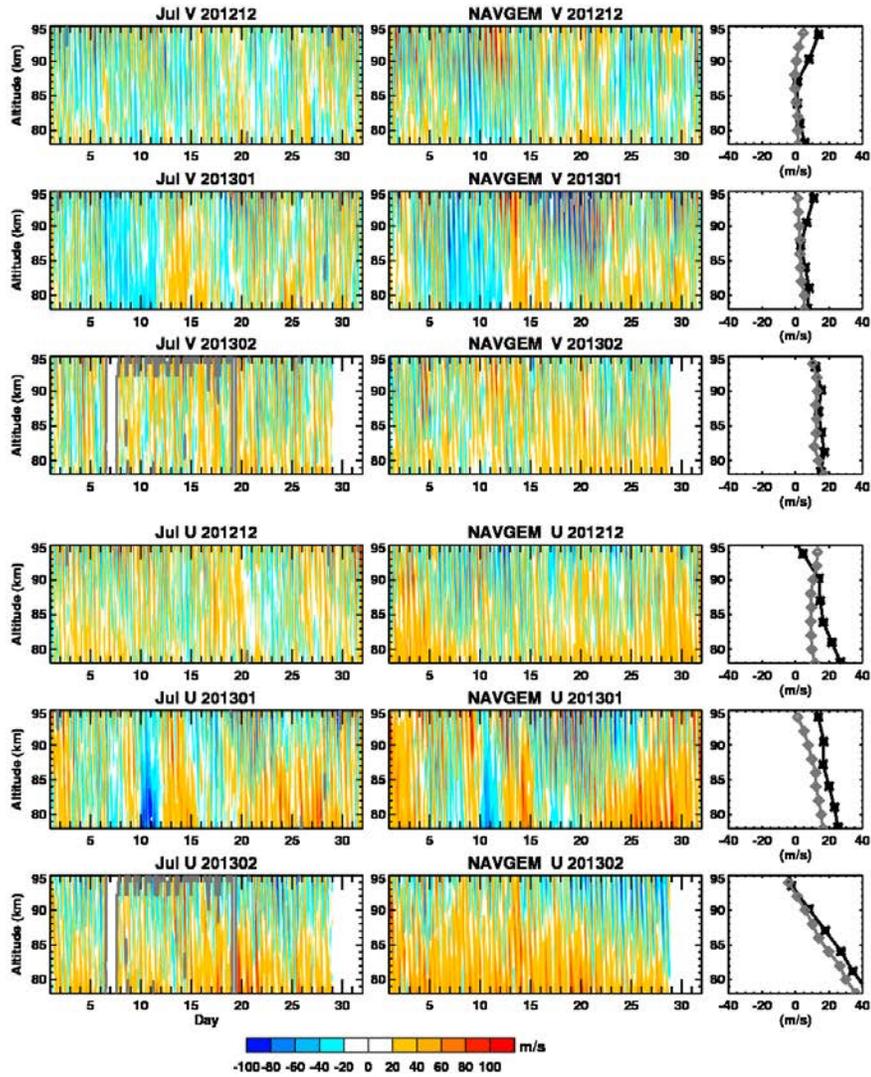


Figure 9: As in Figure 8 but for the 2012-2013 winter.

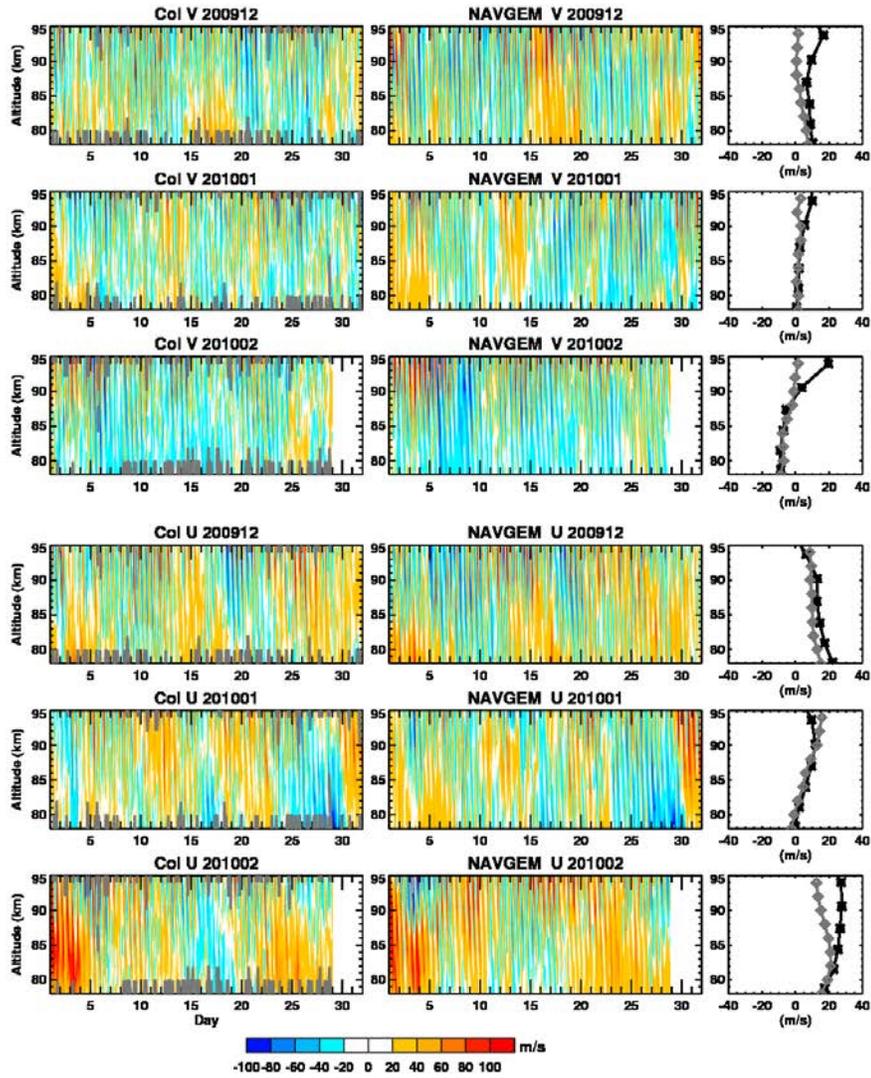


Figure 10: Meridional and zonal winds from meteor radar observations (left column) and NAVGEM analyses (center column) at Collm for the 2009–2010 winter. Gray contours denote missing data. Corresponding monthly mean wind profiles (right column) from NAVGEM (black stars) and meteor radar observations (gray diamonds).

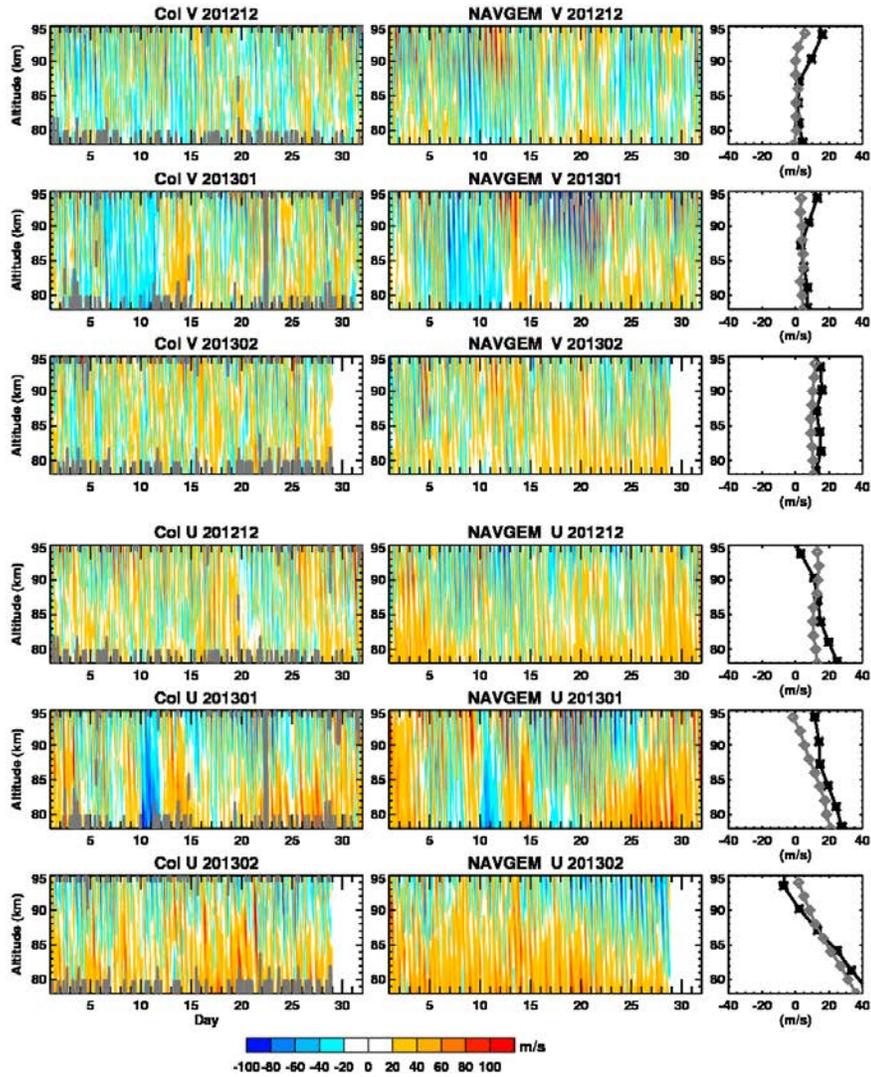


Figure 11: As in Figure 10 but for the 2012–2013 winter.

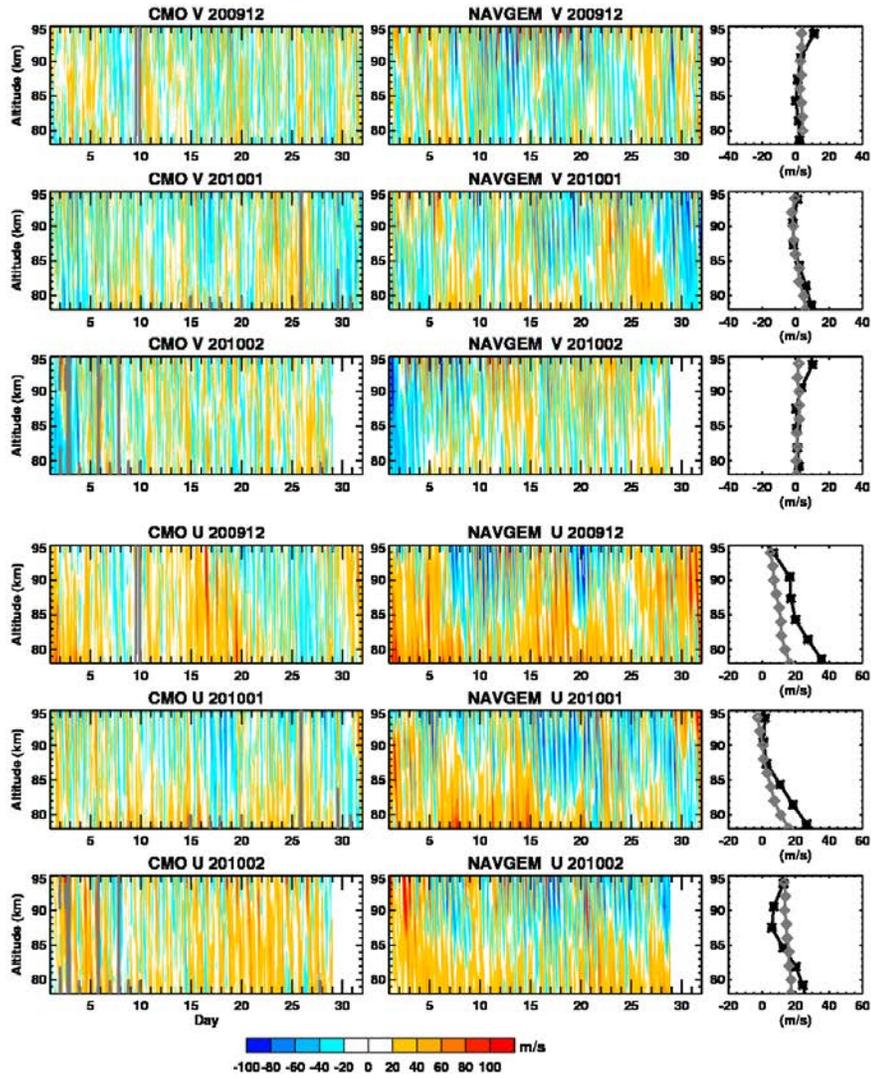


Figure 12: Meridional and zonal winds from meteor radar observations (left column) and NAVGEM analyses (center column) at the CMOR site for the 2009–2010 winter. Gray contours denote missing data. Corresponding monthly mean wind profiles (right column) from NAVGEM (black stars) and meteor radar observations (gray diamonds).

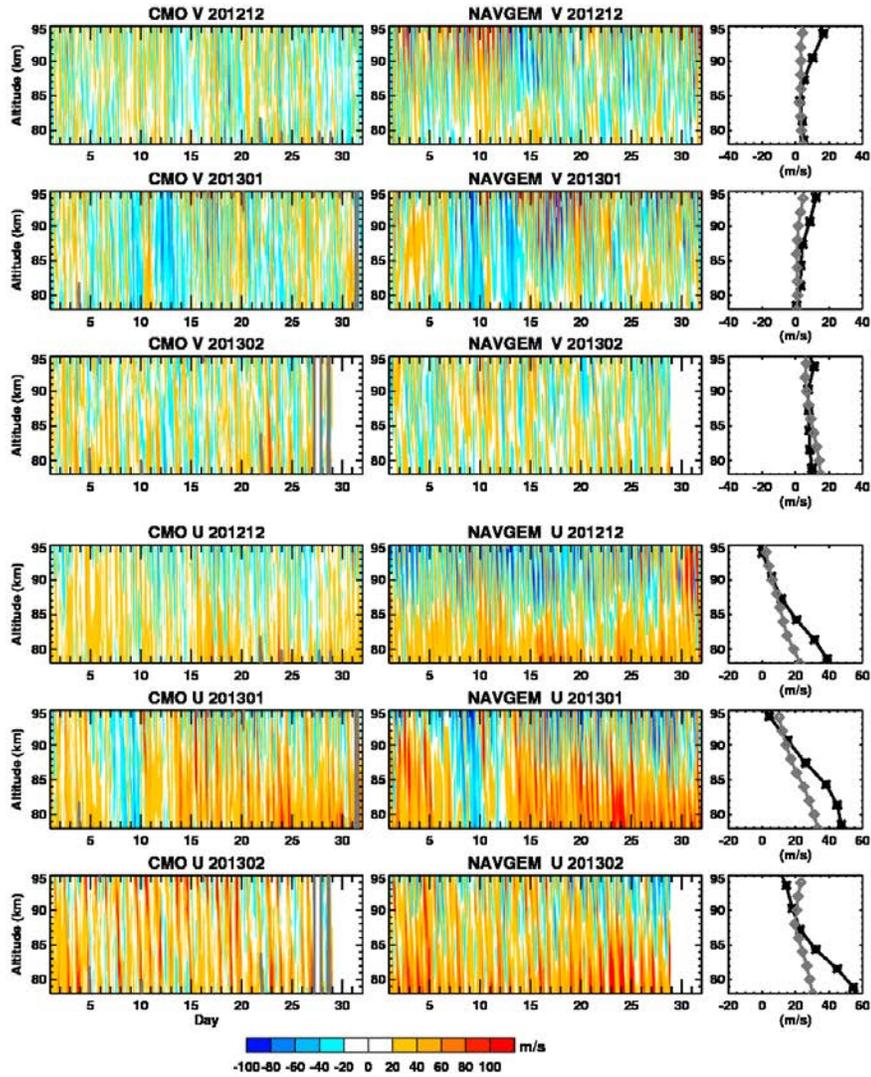


Figure 13: As in Figure 12 but for the 2012–2013 winter.

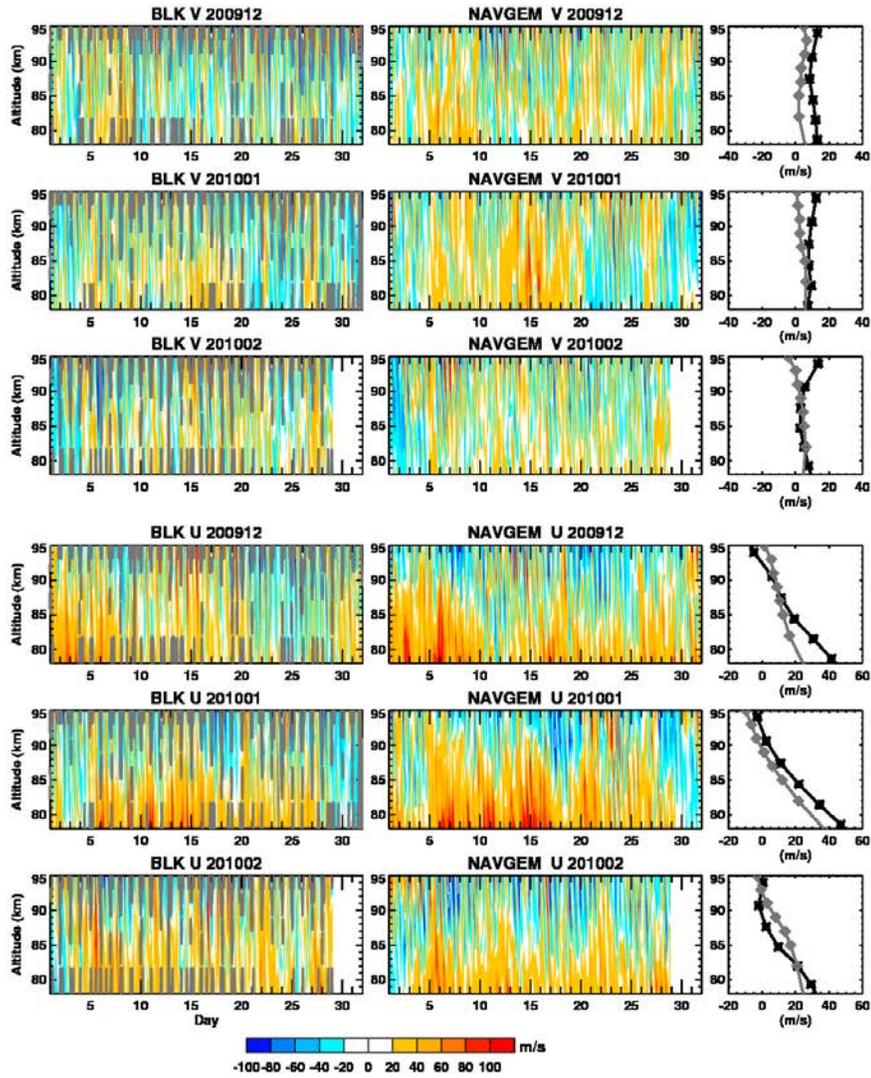


Figure 14: Meridional and zonal winds from meteor radar observations (left column) and NAVGEM analyses (center column) at Bear Lake for the 2009–2010 winter. Gray contours denote missing data. Corresponding monthly mean wind profiles (right column) from NAVGEM (black stars) and meteor radar observations (gray diamonds).

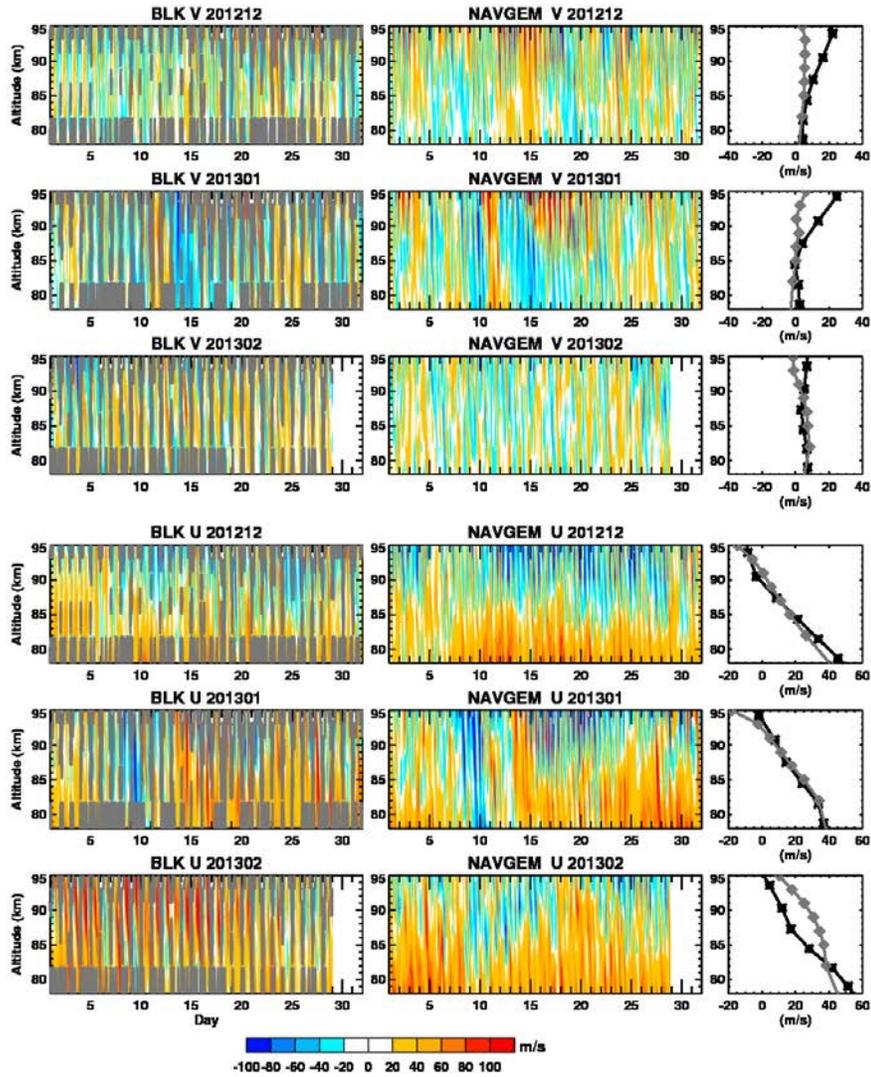


Figure 15: As in Figure 14 but for the 2012–2013 winter.

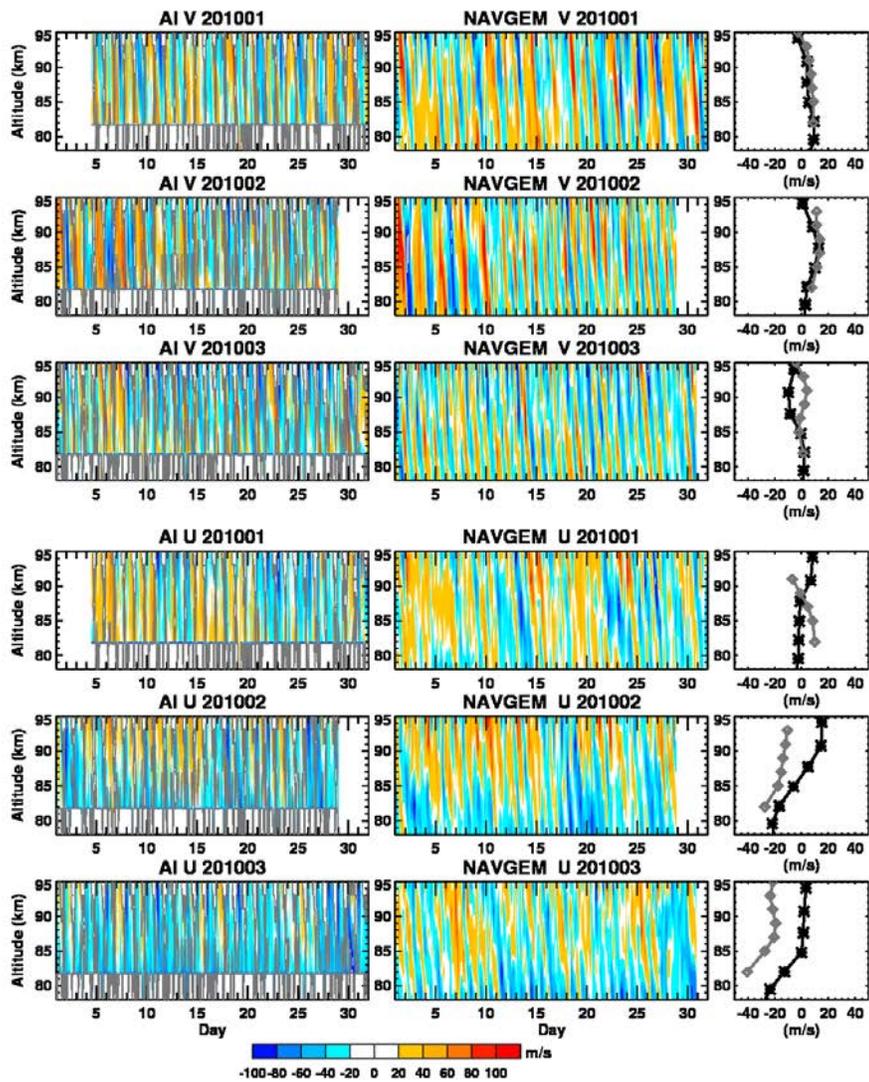


Figure 16: Meridional and zonal winds from meteor radar observations (left column) and NAVGEM analyses (center column) at Ascension Island for the period 1 Jan. – 31 Mar. 2010. Gray contours denote missing data. Corresponding monthly mean wind profiles (right column) from NAVGEM (black stars) and meteor radar observations (gray diamonds).

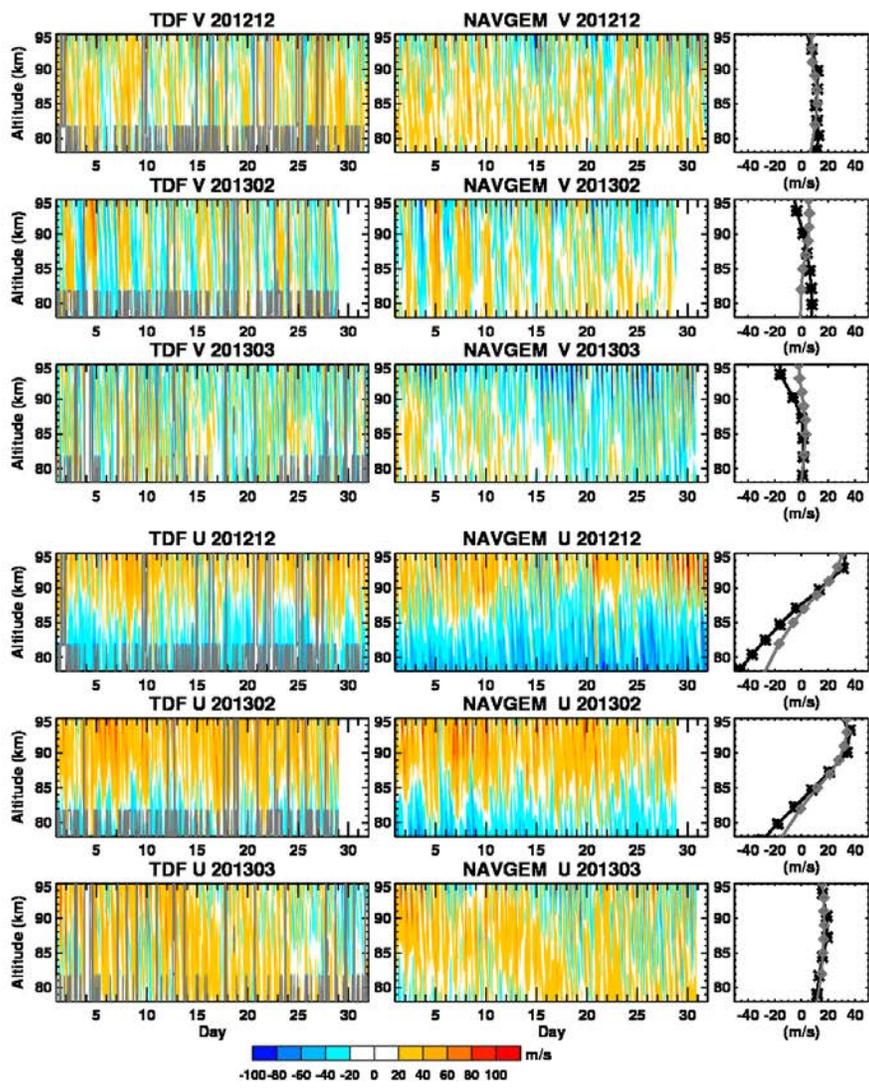


Figure 17: As in Figure 16 but for winds at Tierra del Fuego during 1 – 31 Dec. 2012 and 1 Feb. – 31 Mar. 2013.

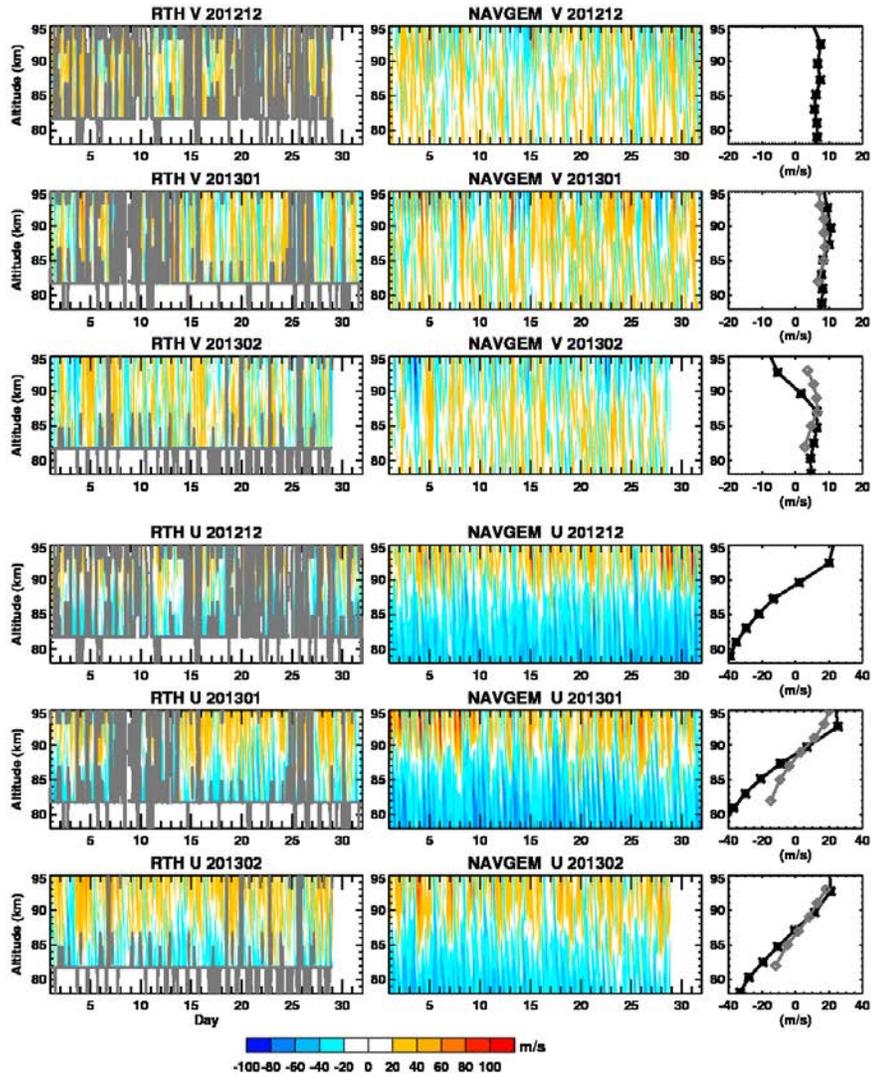


Figure 18: As in Figure 16 but for winds at Rothera from 1 Dec. 2012 – 28 Feb. 2013.

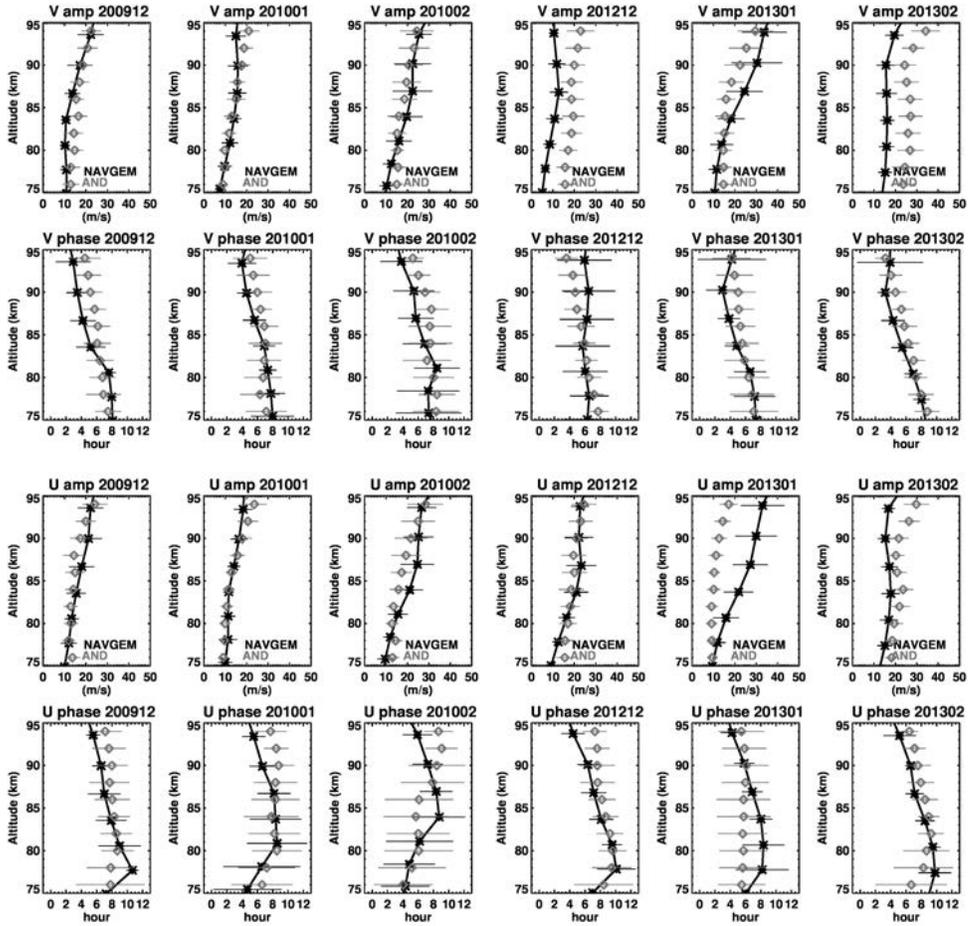


Figure 19: Time averaged vertical profiles of semi-diurnal amplitude and phase in meridional wind (top two rows) and zonal wind (bottom two rows) from NAVGEM (black stars) and meteor radar winds (gray diamonds) at Andenes over the 2009–2010 and 2012–2013 NH winter periods listed in Table 1. Error bars represent the standard deviation about the time mean.

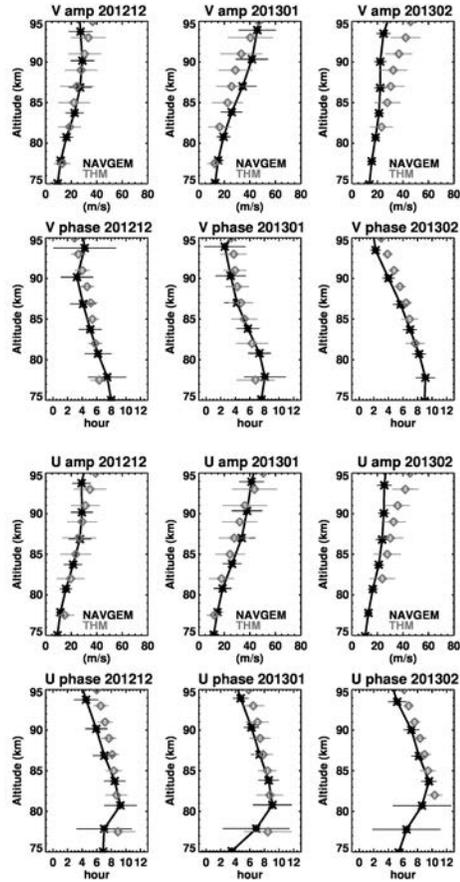


Figure 20: Time averaged vertical profiles of semi-diurnal amplitude and phase in meridional wind (top two rows) and zonal wind (bottom two rows) from NAVGEM (black stars) and meteor radar winds (gray diamonds) at Trondheim over the 2012–2013 NH winter period listed in Table 1. Error bars represent the standard deviation about the time mean.

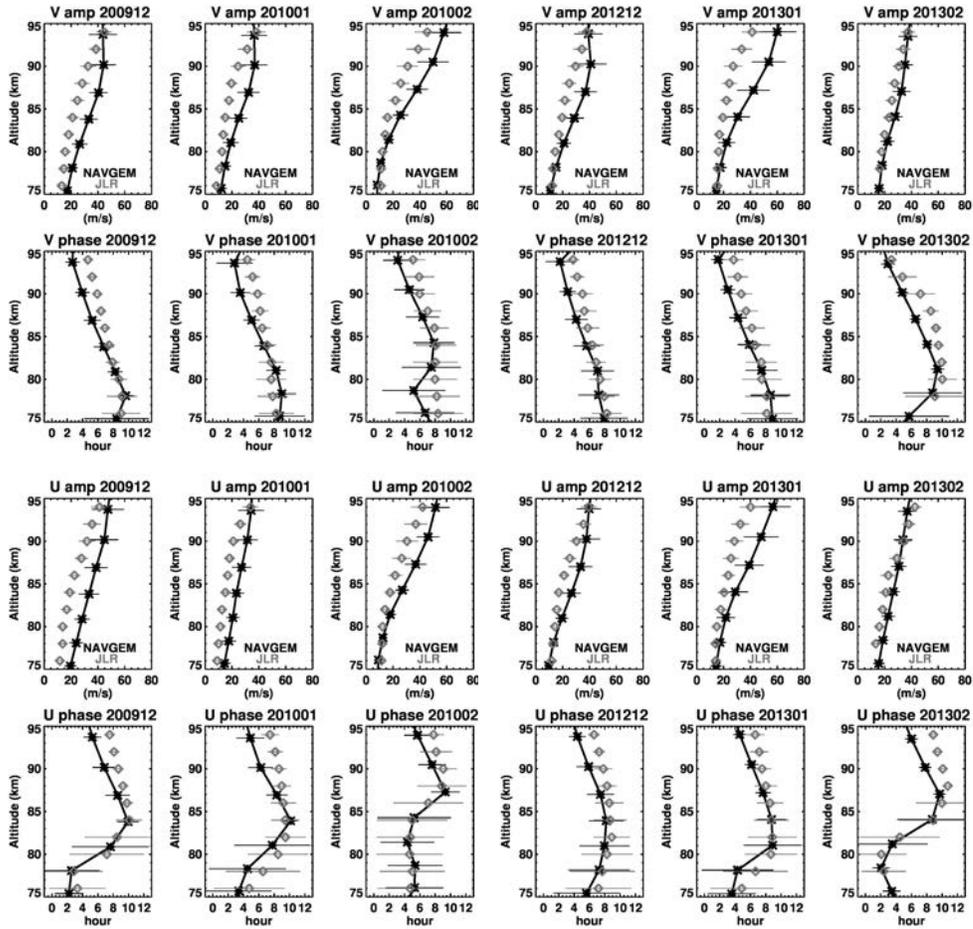


Figure 21: Time averaged vertical profiles of semi-diurnal amplitude and phase in meridional wind (top two rows) and zonal wind (bottom two rows) from NAVGEM (black stars) and meteor radar winds (gray diamonds) at Juliusruh over the 2009–2010 and 2012–2013 NH winter periods listed in Table 1. Error bars represent the standard deviation about the time mean.

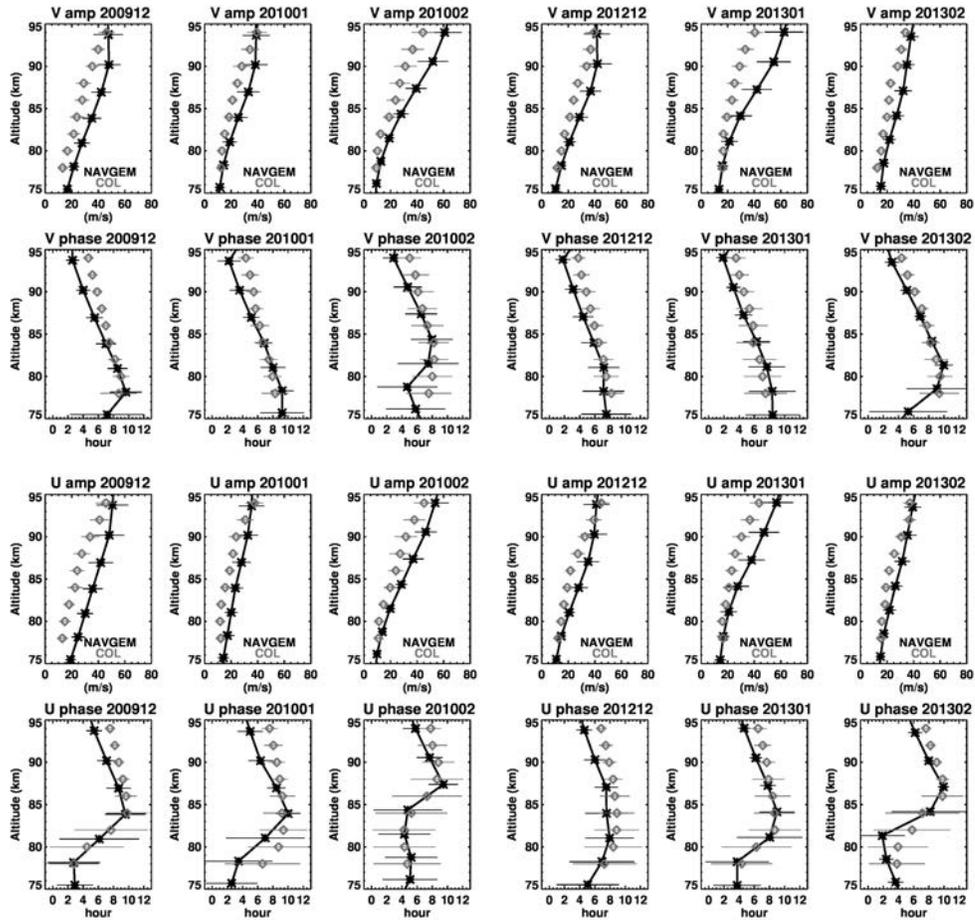


Figure 22: As in Fig. 21 but for Collm.

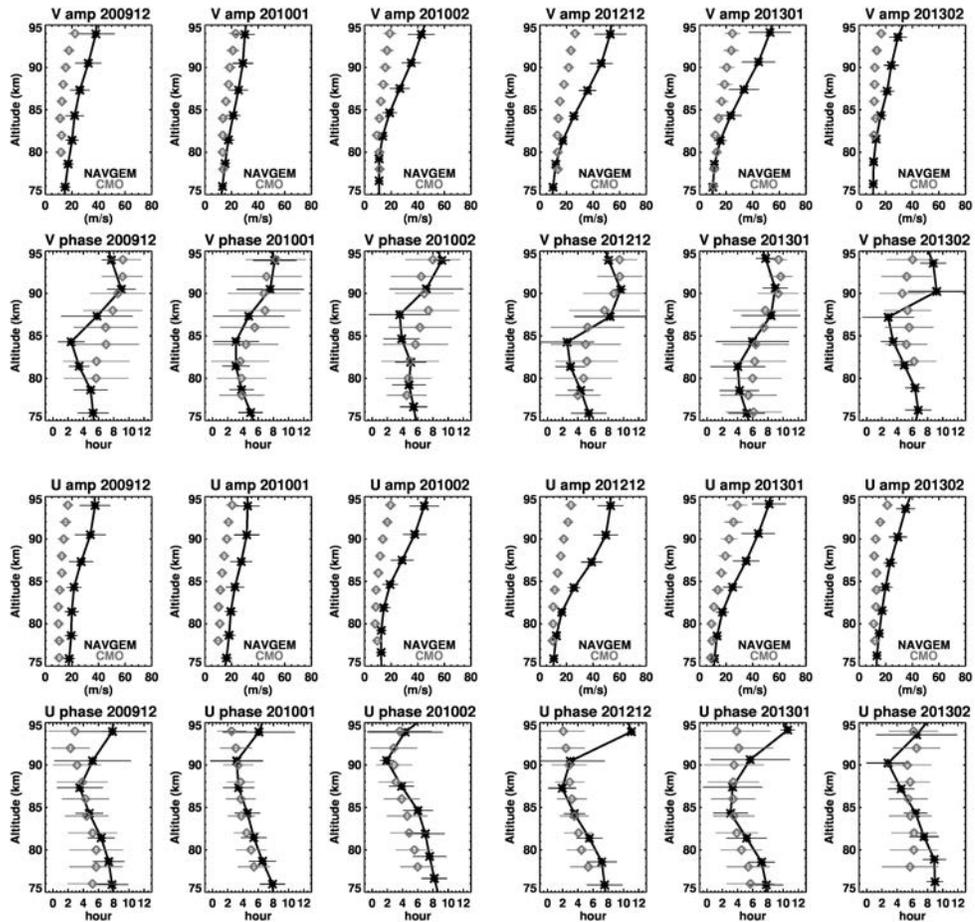


Figure 23: As in Fig. 21 but for the Canadian Meteor Orbit Radar.

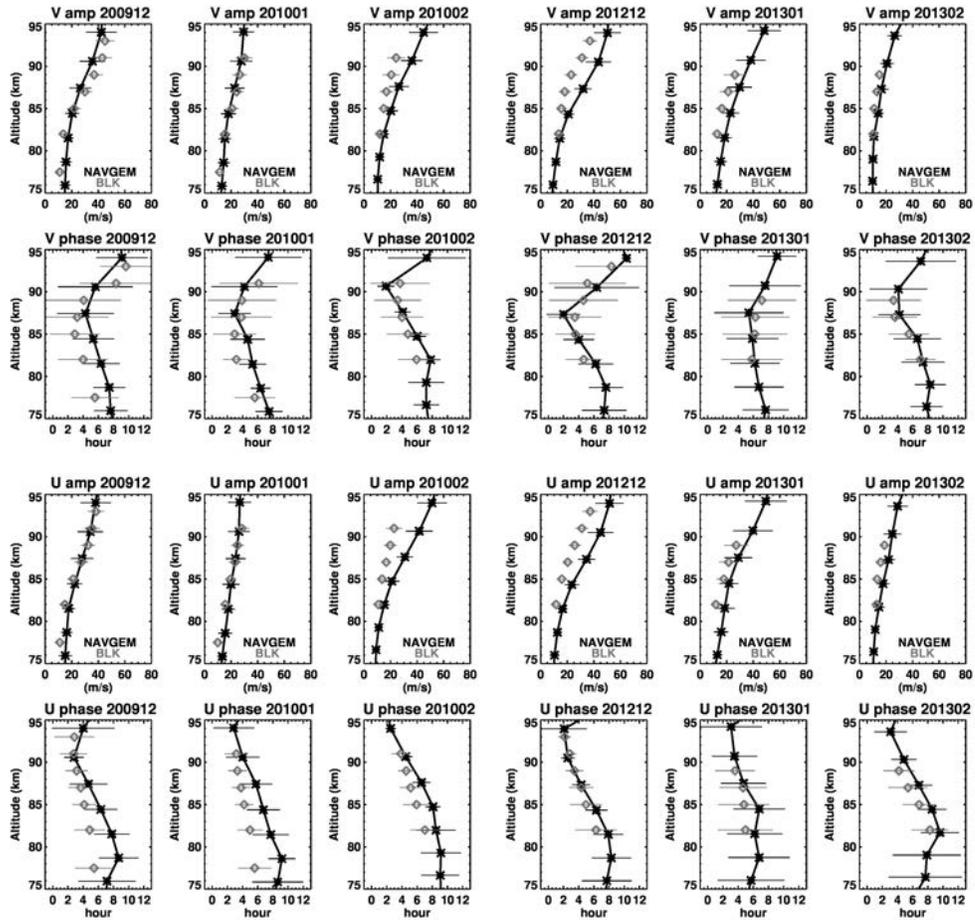


Figure 24: As in Fig. 21 but for Bear Lake.

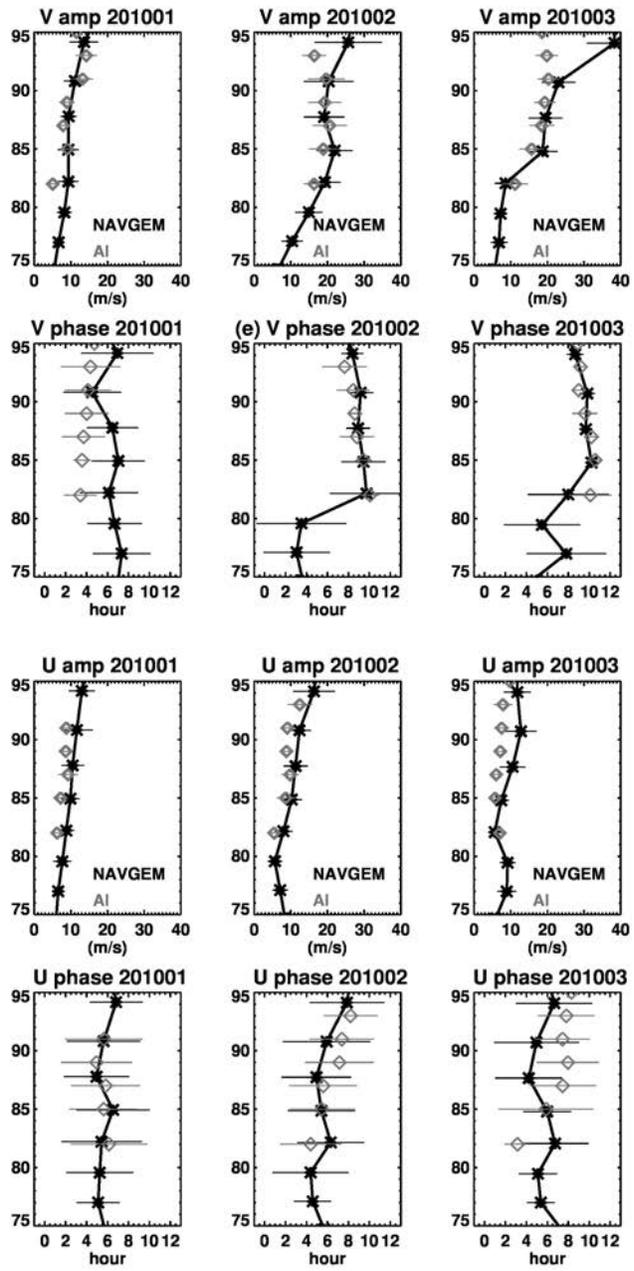


Figure 25: As in Fig. 21 but for Tierra del Fuego for the December 2012 and February–March 2013 periods listed in Table 1.

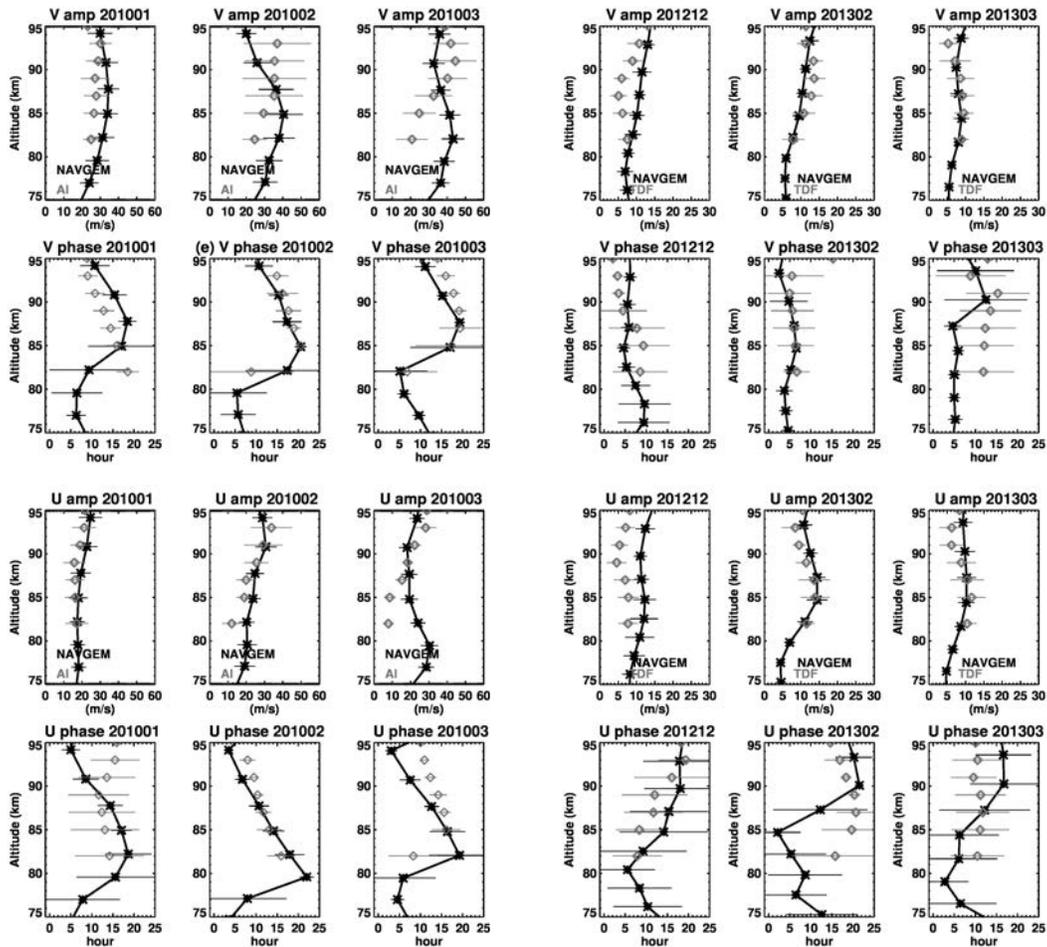


Figure 26: Time averaged vertical profiles of diurnal amplitude and phase in meridional wind (top two rows) and zonal wind (bottom two rows) from NAVGEM (black stars) and meteor radar winds (gray diamonds) at Ascension Island over the January – March 2010 period (left) and at Tierra del Fuego for the December 2012 and February–March 2013 periods listed in Table 1. Error bars represent the standard deviation about the time mean.

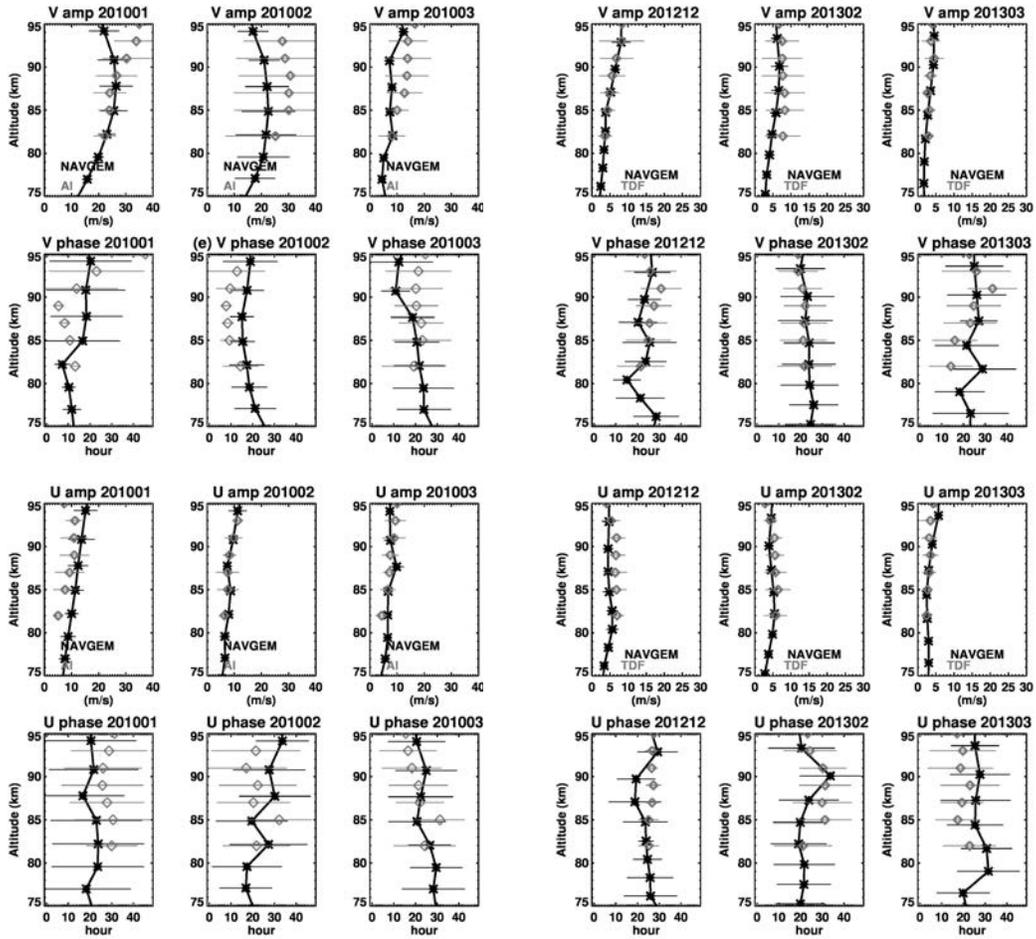


Figure 27: Time averaged vertical profiles of quasi-2 day amplitude and phase in meridional wind (top two rows) and zonal wind (bottom two rows) from NAVGEM (black stars) and meteor radar winds (gray diamonds) at Ascension Island over the January – March 2010 period (left) and at Tierra del Fuego for the December 2012 and February–March 2013 periods listed in Table 1. Error bars represent the standard deviation about the time mean.

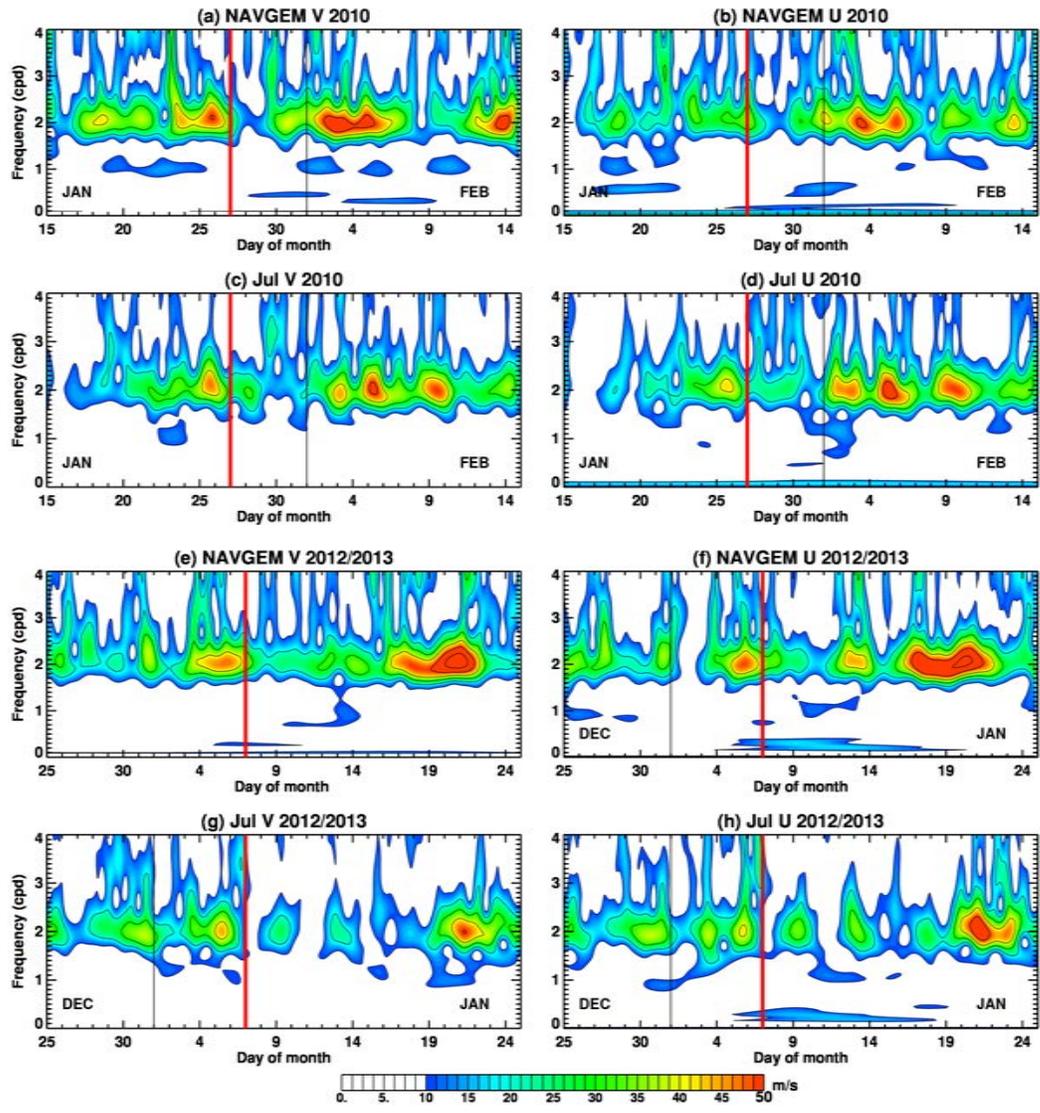


Figure 28: Time-frequency plots of meridional and zonal wind amplitudes  $|S|$  derived from NAVGEM and radar winds for Juliusruh over the periods of 15 January – 15 February 2010 (a-d) and 25 December 2012 – 25 January 2013 (e-h). Red vertical line denotes the onset of mesospheric easterly flow on 27 January 2010 and 7 January 2013, as indicated in Fig. 1. Contours are drawn every  $10 \text{ m s}^{-1}$ .

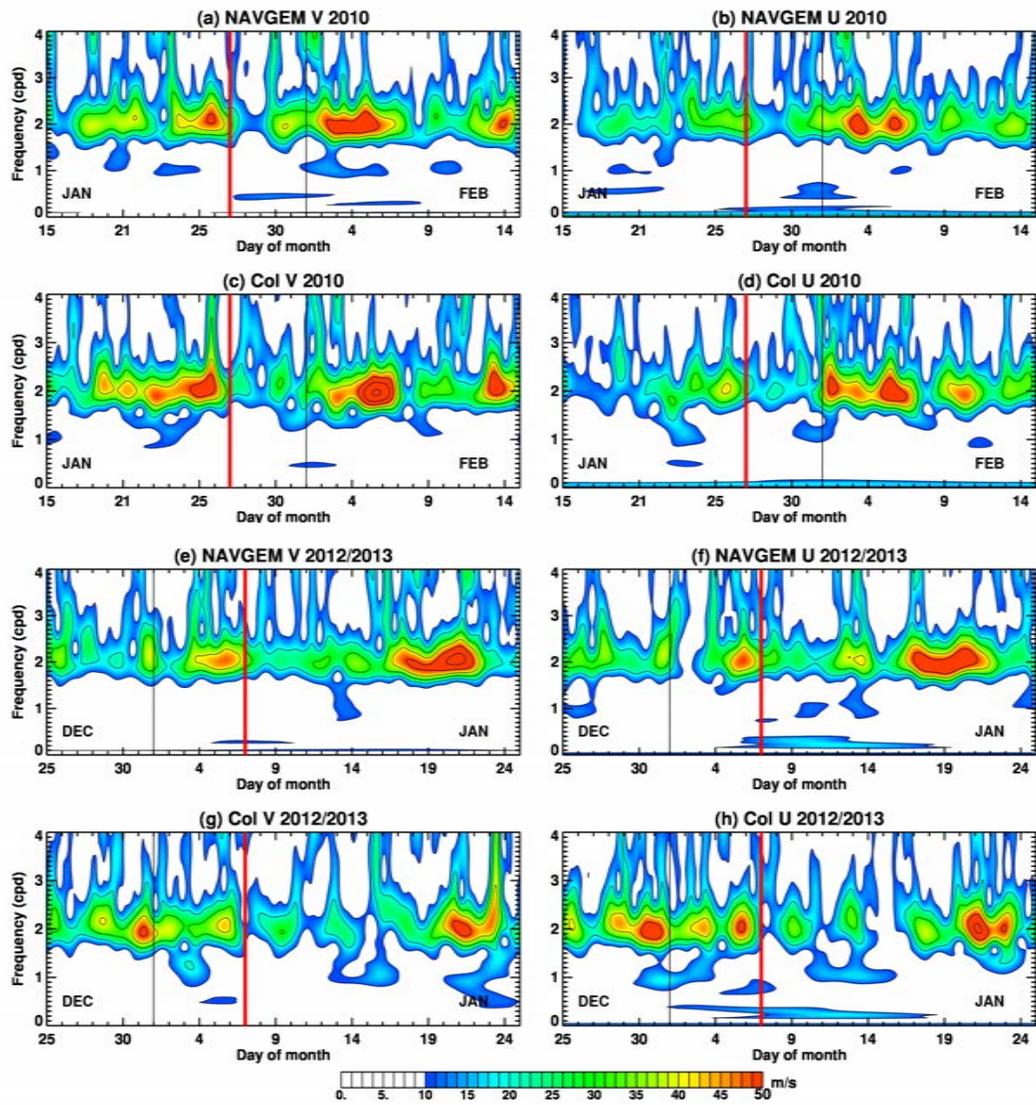


Figure 29: As in Fig. 28 but for Collm.

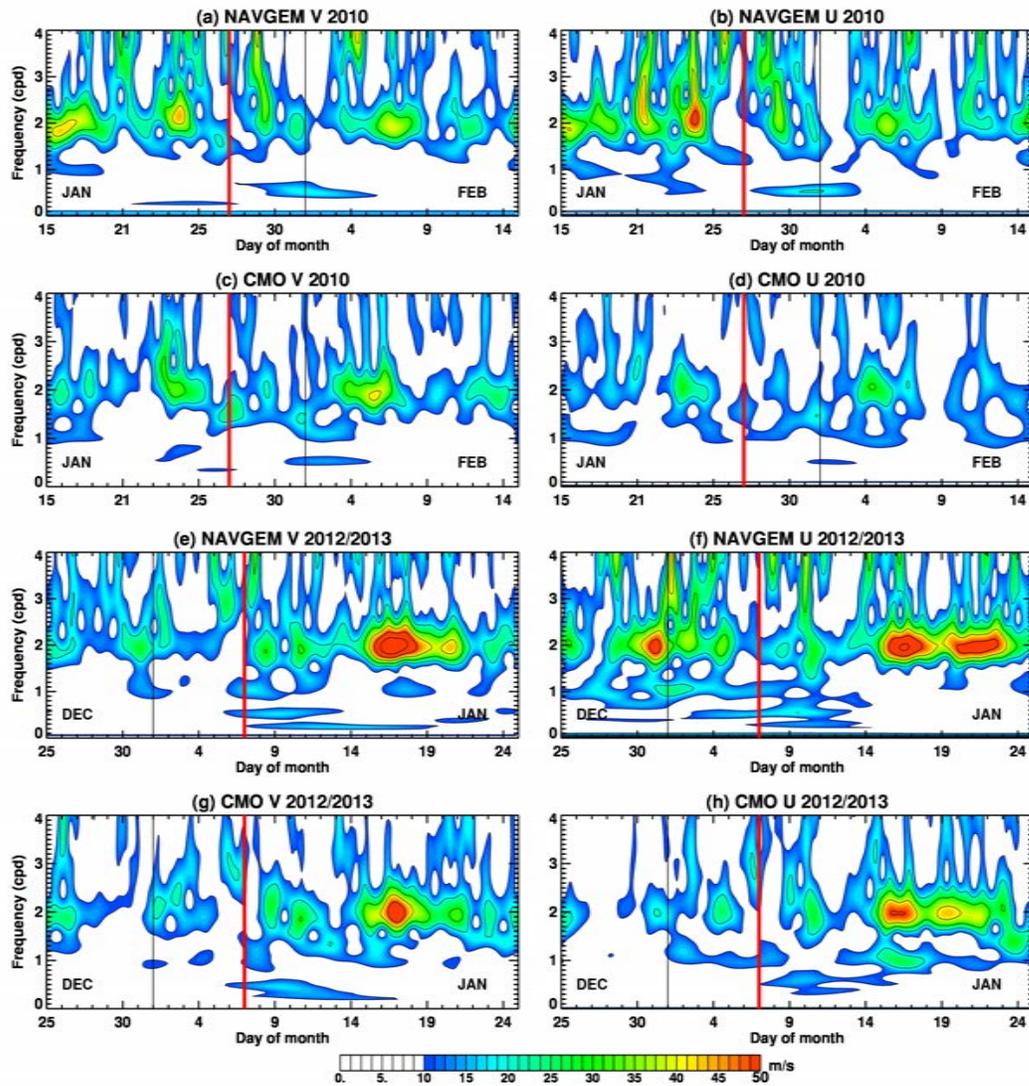


Figure 30: As in Fig. 28 but for the CMOR site.

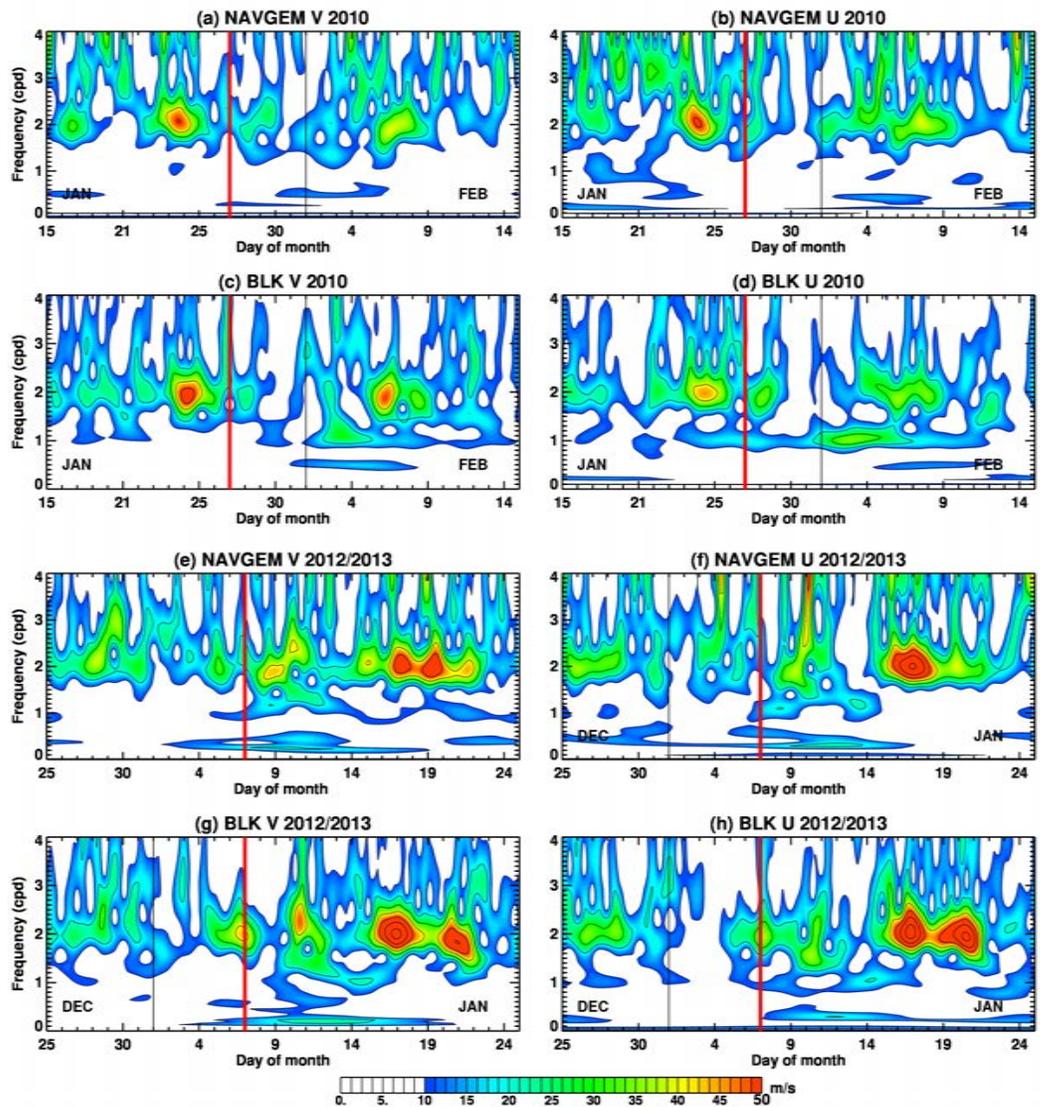


Figure 31: As in Fig. 28 but for Bear Lake at 87 km.

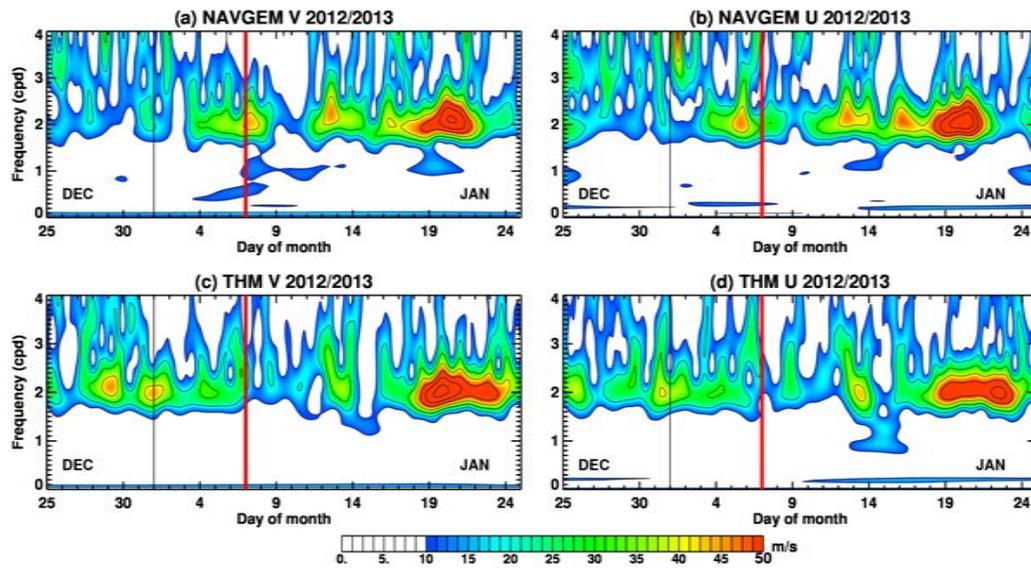


Figure 32: Time-frequency plots of meridional and zonal wind amplitudes  $|S|$  derived from NAVGEM and radar winds for Trondheim over the period 25 December 2012 – 25 January 2013. Red vertical line denotes the onset of mesospheric easterly flow on 7 January 2013, as indicated in Fig. 1. Contours are drawn every  $10 \text{ m s}^{-1}$

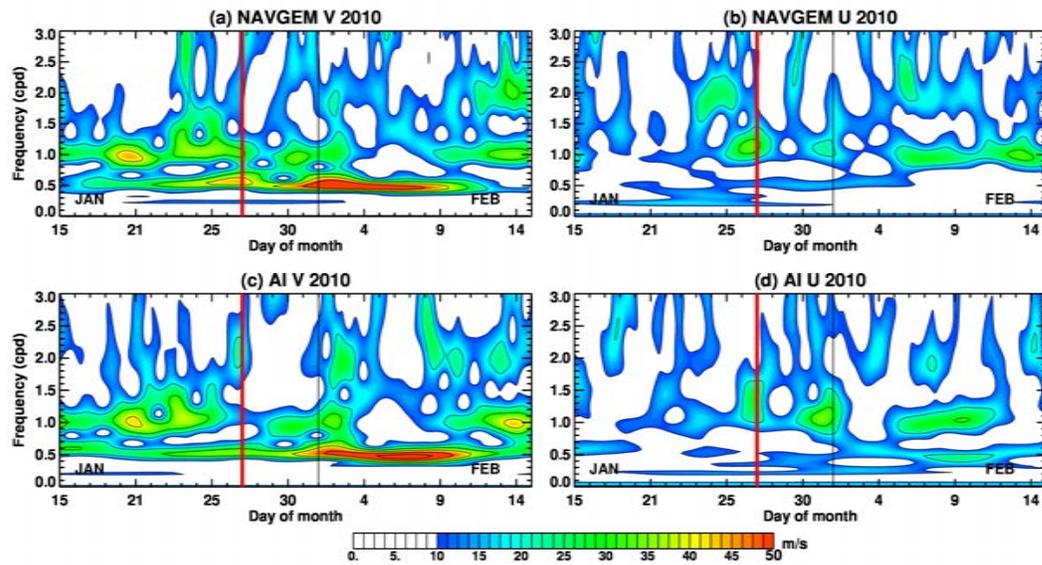


Figure 33: Time-frequency plots of meridional and zonal wind amplitudes  $|S|$  derived from NAVGEM and radar winds for Ascension Island over the period 15 January – 15 February 2010. Red vertical line denotes the onset of mesospheric easterly flow on 27 January 2010, as indicated in Fig. 1. Contours are drawn every  $10 \text{ m s}^{-1}$ .

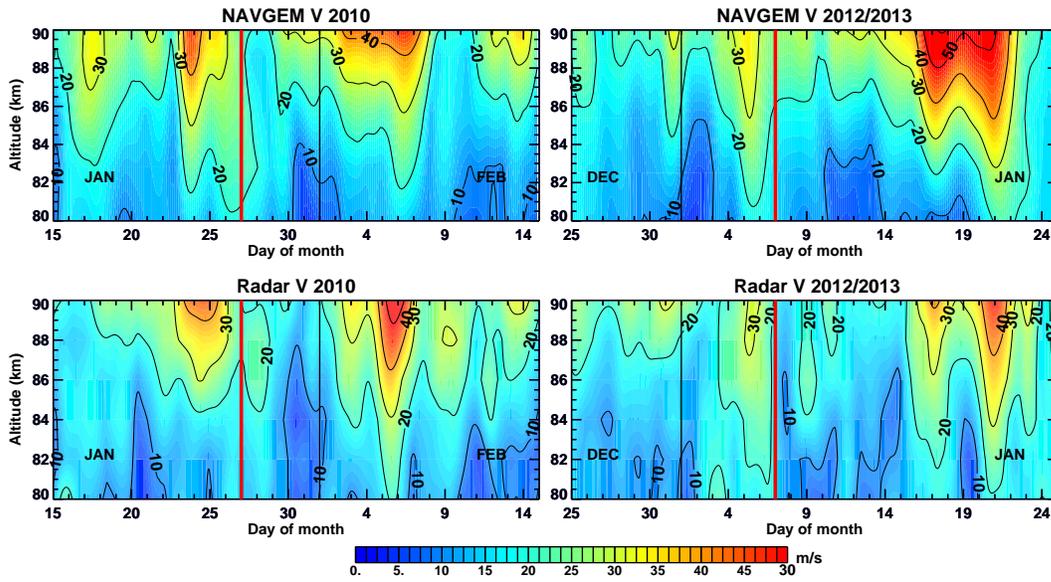


Figure 34: Altitude-time variations in semi-diurnal amplitudes from NAVGEM (top) and radar (bottom) meridional winds averaged over the locations of the Northern Hemisphere extratropical sites listed in Table 1 for the periods 15 January – 15 February 2010 (left column) and 25 December 2012 – 25 January 2013 (right column). red vertical lines denote the onset of mesospheric easterly flow on 27 January 2010 and 7 January 2013. Contours are drawn every  $10 \text{ m s}^{-1}$ .